3-2020

The Design of a Continuous Wave Molecular Nitrogen Stimulated Raman Laser in the Visible Spectrum

Timothy J. Bate

The Design of a Continuous Wave Molecular Nitrogen Stimulated Raman Laser in the Visible Spectrum

THESIS

Timothy J. Bate, 1st Lt, USAF

AFIT-ENP-MS-20-078

DEPARTMENT OF THE AIR FORCE
AIR UNIVERSITY

AIR FORCE INSTITUTE OF TECHNOLOGY

Wright-Patterson Air Force Base, Ohio

AFIT-ENP-MS-20-078

THE DESIGN OF A CONTINUOUS WAVE MOLECULAR NITROGEN STIMULATED RAMAN LASER IN THE VISIBLE SPECTRUM

THESIS

Presented to the Faculty

Department of Engineering Physics

Graduate School of Engineering and Management

Air Force Institute of Technology

Air University

Air Education and Training Command

in Partial Fulfillment of the Requirements for the

Degree of Master of Science in Applied Physics

Timothy J. Bate, B.S. Electrical Engineering and B.S Computer Engineering

1st Lt, USAF

February 25, 2020

AFIT-ENP-MS-20-078

THE DESIGN OF A CONTINUOUS WAVE MOLECULAR NITROGEN STIMULATED RAMAN LASER IN THE VISIBLE SPECTRUM

THESIS

Timothy J. Bate, B.S. Electrical Engineering and B.S Computer Engineering
1st Lt, USAF

Committee Membership:

Dr. Christopher A. Rice
Chair

Dr. Glen P. Perram
Member

Dr. Ben Pulford
Member

Dr. Greg Pitz
Member

AFIT-ENP-MS-20-078

Abstract

Power scaling in solid core fibers in the near infrared and farther are approaching fundamental limits defined by nonlinear processes. Gas cell systems suffer from failure to maintain high intensities in the large volumes needed in high power systems. Hollow-core photonic crystal fibers (HCPCFs) shows promise as a hybrid laser with higher nonlinear process limits and small beam size over long gain lengths. Continuous wave(CW) operation of gas-filled HCPCFs have a few demonstrations, which is only the first step toward demonstrating the potential scaling. This work focuses on the design of a CW molecular nitrogen (N_2) stimulated Raman laser. N_2 offers Raman gains scaling up to 900 amg, particularly scaling higher than the more studied H_2 which stops scaling at 14 amg. An overview of stimulated Raman scattering and HCPCFs, a 2-mirror cavity experiment, and an HCPCF experiment provided insights into an update to previous models used for vibrational Raman. The cavity experiment showed the need to include Rayleigh scattering in the high pressure environments required for N_2 Raman lasing. The HCPCF experiment showed limitations due to chamber leaks which caused the fiber end to move out of alignment with the pump beam. The updated model showed the small beam size and long gain length of the HCPCF configuration is an optimal path toward scaling with N_2 stimulated Raman. Demonstration and scaling appear to be attainable goals with good gas containment for either the cavity or the hollow-core fiber, but HCPCF allows for lower pressures when paired with long low-loss fiber lengths. Even at relatively low pressures such as 1,500 psi, high conversion percentages should be found if the fiber length is chosen based on the pump and gain, 15 m for N_2 at 1500 psi with a predicted 87% conversion of the 4.2 W coupled from the 532 nm pump. This shows promise for moving farther

into the infrared, but more work must be done with understanding coupling to the hollow-core modes.

Acknowledgements

I would like to thank Dr. Christopher Rice for his guidance and countless hours helping me put together and take apart my experimental apparatus. He was always available and helped keep me sane as I dealt with the issues that presented themselves. I could not chosen a better chair to work with me and help me to grow throughout this work. I would like to thank Dr. Perram for his thoughts and insights on the theory and possible explanations for it for many pieces of this work. I would also like to thank fellow student Josh Key for helping with some muscle over Christmas quarter break. I would also like to thank the friends and family members who supported me in reading through my document for typos as well as their emotional support.

Timothy J. Bate

Table of Contents

List of Figures

Figure Page

THE DESIGN OF A CONTINUOUS WAVE MOLECULAR NITROGEN STIMULATED RAMAN LASER IN THE VISIBLE SPECTRUM

I. Introduction

The Department of Defense (DoD) has been interested in the use of high energy laser weapons for many decades. The Airborne Laser, the Tactical High Energy Laser, and Large Aircraft Infrared Countermeasures are a few examples. [5] The two main paths forward in this venture are thought to be silica-based solid core doped fiber amplifiers and alkali gas cell lasers. [6] Each of these laser design schemes have strengths and have significant limitations as a path forward. The solid-core fiber solution allows for long gain path lengths of high-intensity pump light and all-fiber systems spliced together which results in a rugged system. The limitations result from the heating of the fibers, which requires significant amounts of cooling, and non-linear processes which fundamentally limit the power-scaling capacity of any single fiber. Scaling in gas cells is not traditionally limited by these non-linear process due to the orders of magnitude higher thresholds. However, the lack of ability to maintain high intensities throughout the gain does require bigger gas cells. In the last twenty years, an opportunity to combine the strengths of both of these paths has been developing, the hollow-core photonic crystal fiber (HCPCF). A detailed history of the developments in HCPCFs can be found in Debord et al. [7]

The HCPCF allows for high-intensity, long gain path length, small size and high non-linear process limits. Many lasers have been built from gas-filled HCPCFs from either standard gas transitions, typically referred to as a hollow-core optical fiber gas laser (HOFGLAS), or Stimulated Raman Scattering (SRS). [8, 9, 10, 4, 11, 12, 13,

14, 15, 16, 17, 18, 19] HOFGLASs typically suffer from laser emission at atmospheric absorption lines or from issues with maintaining uniform gain throughout the fiber such as with condensing gain media like alkalis. SRS lasers can be designed to avoid these problems as the lasing wavelength is a linear offset from the pump wavelength based of the gas used. This allows for the use of standard atmospheric gases such as hydrogen and nitrogen.

In this work, a single pass through a gas cell was used to image the Rayleigh and Raman scattering. Following the initial test, a gas cell high-Q cavity and a HCPCF filled with nitrogen gas were each used as methods for achieving continuous wave(CW) SRS lasing at varying pressure in the visible regime of the optical spectrum to determine feasibility of nitrogen as a gain media for a Raman CW laser. The N_2 was tested with pressures up to 3500 psi due to gas containment limitations of the chamber used. By testing both the high-Q cavity and the HCPCF, a more thorough suggestion of the best path forward can be chosen. Nitrogen was chosen due to its Raman Q-branch line narrowing to number densities greater than 800 amagats. [2] This leads to possible Raman gains nearly twice that of more popular hydrogen gas media. Many challenges arise from containing the gas at high pressures with some such challenges discussed later. One large benefit of nitrogen gas is that it does not pose a serious combustion risk or inhalation risk as a mostly inert gas. These high pressures did introduce losses from Rayleigh scattering, which has been largely ignored in previous works due their lower number densities.

Background on SRS in high-Q cavities and in HCPCFs will be given as a foundation. Experiments in hydrogen gas will be discussed, having been much more thoroughly investigated than nitrogen. An overview of previous work in these areas from a number of authors will be discussed including most SRS HCPCF work in the last half decade starting in 2002 with a critical demonstration in hydrogen by

Benabid et al. [16] While SRS of hydrogen in high-Q cavities has been much more thoroughly researched over several decades due to its high energy shift, relatively high gain, and more established laser gain setup, SRS in nitrogen has been rarely studied due to the low Raman gain at low pressures under 1500 psi. A short overview of the experimental setup for each of these experiments will be given. The results of those tests will be shown, leading to an update of the current equations used to model SRS in both setups as discussed in the background to better explain what was seen in the experiments. Finally, recommendations on the best decisions for SRS N_2 laser systems will be made from the updated model.

II. Background

2.1 Stimulated Raman

Raman scattering is a non-linear process by which photons are shifted from one frequency to another when interacting with molecules in any state of matter. Some applications see it as a useful tool for investigating the material, while others see it as a loss from the intended goal of those incident photons. Raman spectroscopy uses high frequency light to determine the energy level of the material based on the shift of the light, which allows for identifying it without directly observing the transition lines. Here, it is seen as the desired lasing mechanism. The three levels of a SRS Laser are shown in Fig. 1. The diagram shows the vibrational states of a molecule along with virtual states, but this applies similarly to rotational states. The dashed lines are the virtual state that act as the upper state, which means that it is not a eigenstate solution to the Schrodinger equation. It comes out of perturbation theory as a solution from perturbations caused by inelastic collisions. The transition can either be $|0>$ to $|2>$ to $|1>$, called the Stokes transition, or $|1>$ to $|2>$ to $|0>$, called the Anti-Stokes transition. The Stokes transition leads to a decrease in energy of the pump photon to the emitted photon as in $\nu_s = \nu_p - \frac{E_{shift}}{h}$, where ν_s is the Stokes frequency, ν_p is the pump frequency, E_{shift} is the energy difference between the two vibrational or rotational level, and h is plank's constant. The Anti-Stokes transition does the opposite and increases the frequency as in $\nu_{as} = \nu_p + \frac{E_{shift}}{h}$, where ν_{as} is the Anti-Stokes frequency. The Anti-Stokes line generally has a much higher threshold due to the higher population of the lower level at reasonable temperatures following from a Boltzmann distribution, $e^{-E/kT}$. The energy lost in the Stokes transition is added heat, and the energy gained in the Anti-Stokes results in losing heat. The gain coefficient for Raman transitions is proportional to a differential cross-section with

respect to solid-angle and can be written as

$$\gamma = \left(\frac{\lambda_s^3}{hc}\right)\left(\frac{2}{\pi\Delta\nu}\right)\Delta N\frac{d\sigma}{d\Omega}, \tag{1}$$

where γ is the gain coefficient, c is the speed of light, λ_s is the shifted (Stokes) wavelength, the second term is the Lorentzian line-shape with $\Delta\nu$ being the FWHM, ΔN is the population difference between the initial and final state, and $\frac{d\sigma}{d\Omega}$ is the differential Raman cross-section. [1] This differential cross-section can be described using

$$\frac{d\sigma}{d\Omega} = B\frac{\nu_s^4}{(\nu_i^2 - \nu_p^2)^2}, \tag{2}$$

where ν_s is the Stokes frequency, ν_p is the pump frequency, and B and ν_i are fit parameters defined by the gas in this work. [20] For H_2, A is $8.74 \times 10^{-28}\frac{cm^2}{str}$ and ν_i is $84,800\ cm^{-1}$, while they are $3.02 \times 10^{-28}\frac{cm^2}{str}$ and $89,500\ cm^{-1}$ for N_2, respectively. The vibrational gain coefficients for H_2, N_2 and O_2 can be seen in Fig. 2 and Fig. 3, respectively.

Generally, it can be assumed that the final state in the Stokes transition is approximately empty, and the equation is simplified with the total population, N, instead of ΔN. The number density in amagats is found by $(P/P_0)(T_0/T)$ where P_0 is 1 atm and T_0 is 273 K. SRS offers flexible lasing wavelength by allowing a pump to be chosen to get to a desired output frequency, commonly the first Stokes shift though with more sophisticated designs a higher-order Stokes shift can be utilized. In SRS with linearly polarized or unpolarized light, the vibrational Stokes transition tends to have higher gain and is thus the favored transition particularly at high pressures. [4] In the case of N_2, pressures in excess of 70 psi are sufficient to become dominant. [21] Given these conditions, rate equations can be developed assuming the electric field

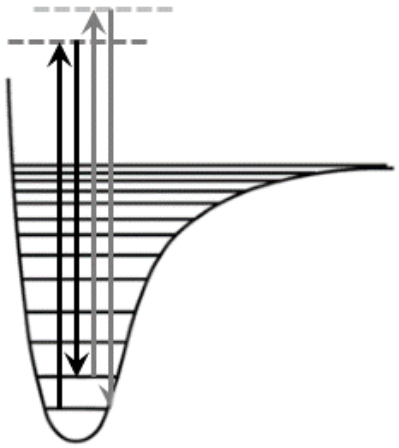

Figure 1. Vibrational Raman transitions shown on top of a Morse Potential curve. (Public Domain). The black transition is the Stokes transition, while the gray transition is the Anti-Stokes transition. The starting position is $\nu = 0$ due to it having the highest population to excite at reasonable temperatures for the Stokes transition or $\nu = 1$ for the Anti-Stokes transition for the same reason.

transitions only between the vibrational Stokes field and the pump field as

$$\frac{dE_s}{dt} = G \mid E_p \mid^2 E_s - L_s E_s \tag{3}$$

$$\frac{dE_p}{dt} = K(E_p^{in}) - \left(\frac{\nu_p}{\nu_s}\right) G \mid E_p \mid^2 E_s - L_p E_p, \tag{4}$$

where the change in each field with respect to time, $\frac{dE_s}{dt}$ and $\frac{dE_p}{dt}$, are defined by the losses to the pump, L_p, losses to the Stokes field, L_s, the pump into the system, $K(E_p^{in})$, and the conversion from pump to Stokes. [15] The conversion from pump to Stokes is related to the pump field squared, $\mid E_p \mid^2$, and the Raman gain defined by

$$G = \sqrt{\frac{\epsilon_0}{\mu_0}} \left(\frac{c\gamma}{8}\right) \left(\frac{\lambda_p}{\lambda_p + \lambda_s}\right), \tag{5}$$

where ϵ_0 is the permittivity of free space and μ_0 is the permeability of free space.

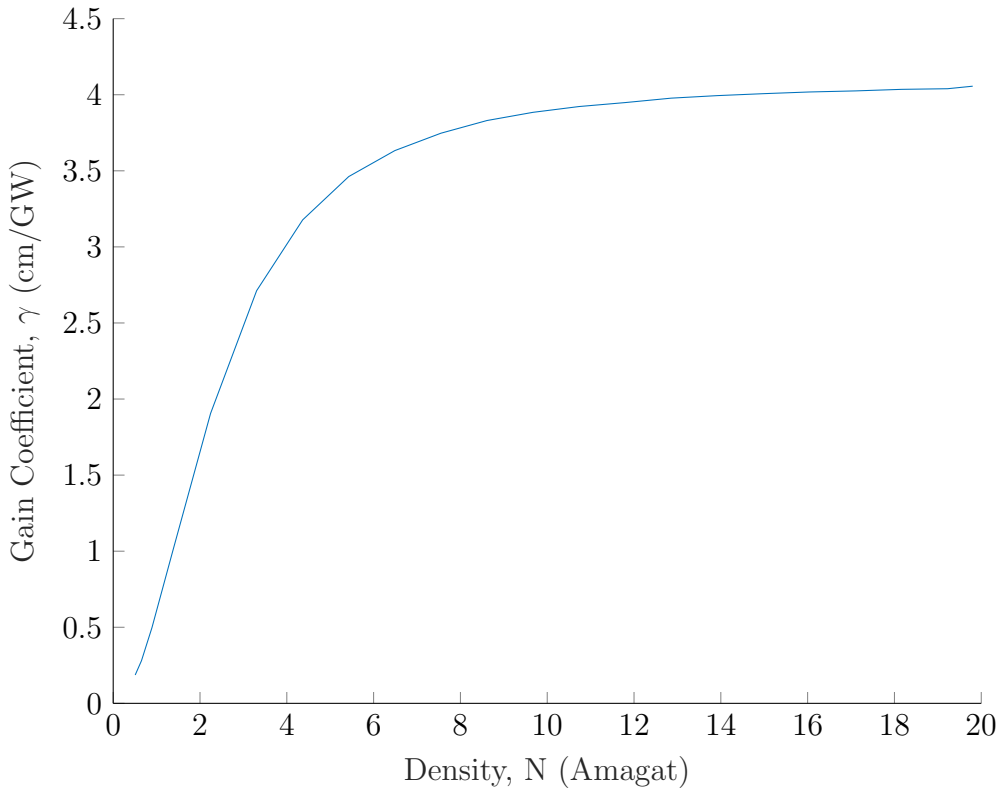

Figure 2. The vibrational gain coefficient of H_2 with respect to number density, which levels off after the Raman linewidth stops collisional narrowing around 10 amagats. Line width data used from Bischel et all. [1]

Solving eq. 3 and eq. 4 will show the Stokes field growth over time. For a more directly measurable quantity, equations for output power can be developed. In the case of a two-mirror cavity, the solution requires only a few extra incites, such as intensity relates to the field by $I = \frac{1}{2}\sqrt{\frac{\epsilon_0}{\mu_0}}\,|E|^2$, the area of the beam is

$$A = \frac{l\lambda_p}{4tan^{-1}\left(\frac{l}{b}\right)} \tag{6}$$

and power relates to intensity by $P = IA$. For the A, l is the cavity length and b is the confocal parameter, defined as

$$b = \sqrt{lr_{ROC}}\sqrt{2 - \frac{l}{r_{ROC}}}, \tag{7}$$

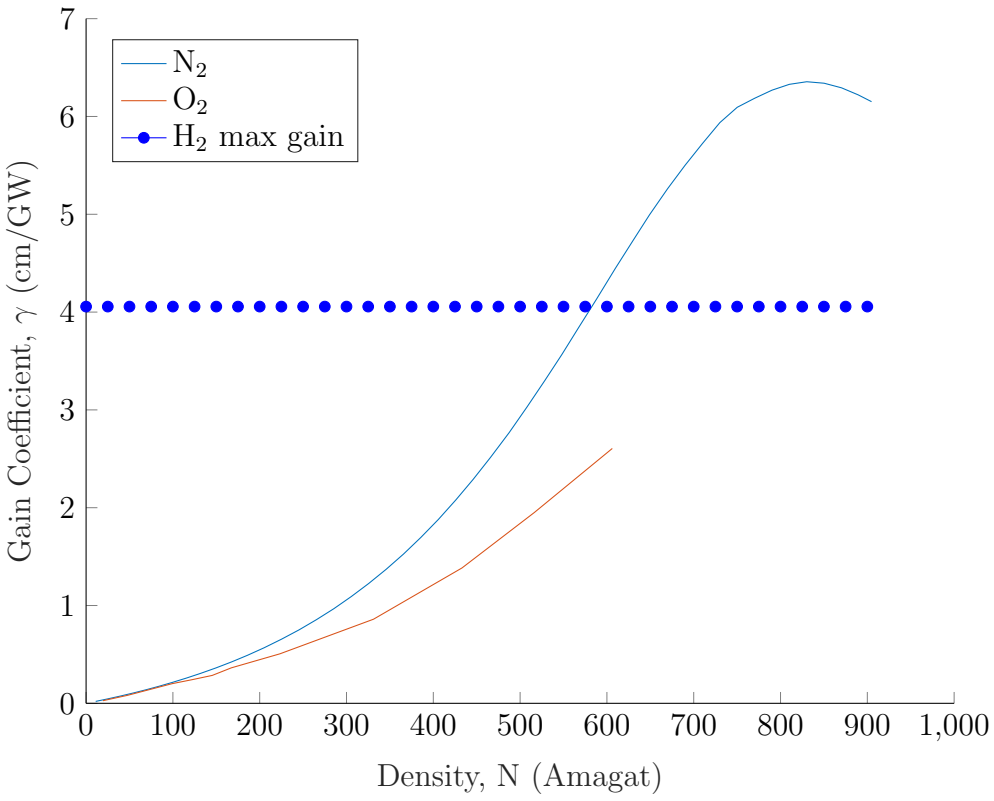

Figure 3. The vibrational gain coefficient of N_2 and O_2 with respect to number density, which levels off after the Raman linewidth stops collisional narrowing around 800 and 600 amagats, respectively. FWHM data from Lavorel et all for nitrogen and Millot et all for oxygen which ends at 600 amagats describes where the curves end. [2, 3] The maximum gain of hydrogen was included as a dotted line for reference.

for a pair of mirrors with shared radius of curvature, r_{ROC}. The losses for each field are

$$L = \frac{c}{2l} ln(\sqrt{R_1 R_2}), \tag{8}$$

where R_1 is the reflectivity of the front mirror and R_2 is the same for the back mirror, not likely the same for each field. Putting it all together, the threshold power is found as

$$P_{th} = \frac{1}{2}\sqrt{\frac{\epsilon_0}{\mu_0}} \left(\frac{A}{G}\right) \left(\frac{L_s L_p l}{c\sqrt{T_{p1}}}\right), \tag{9}$$

where T_{p1} is the transmission of the pump field through the front mirror. [15] The

output Stokes power follows

$$P_{out} = P_0(\sqrt{\frac{P_{in}}{P_{th}}} - 1), \tag{10}$$

where P_0 is a scaling factor defined with transmission of the Stokes field through the back mirror, T_{s2}, as

$$P_0 = (\frac{\nu_p}{\nu_s})\frac{1}{2}\sqrt{\frac{\epsilon_0}{\mu_0}}(\frac{A}{G})(\frac{T_{s2}L_p}{4}). \tag{11}$$

2.2 Hollow-core photonic crystal fiber

Fibers are often used as delivery mechanisms or gain media for laser systems due to their wave-guiding ability, which allow for high intensities over long path lengths. Traditionally, fibers are made from doped silica with an inner core with a high index of refraction and an outer cladding with lower index of refraction; this allows the fiber to guide the light via total internal reflection (TIR). Typically, fibers are made of silica and thus limited by silica absorption in mid-wave infrared and long-wave infrared. They are also limited by dissipating the heat from several non-linear effects such as SRS, Stimulated Brillouin Scattering (SBS), and thermal lensing. One way to increase the threshold set by these non-linear effects is to use a HC-PCF, which can result in dramatic room for improvements in power as seen in table 1, where a 10 m fiber with a 40 μm core pumped at 1.5 μm with a linewidth of 1 GHz was assumed. The HOFGLAS data is taken from Nampoothiri et al and does not include either the pump linewidth described above or a known separate linewidth for the SBS limit due to it being unstated. [22] The solid core and SBS in the N_2 were calculated using equations from Dawson et al with modifications to SBS for on linewidth from Supradeepa. [23, 24] The SBS gain in N_2 with pressure was determined from Renninger et al and Yang et al. [25, 26] N_2 material damage is the laser-induced breakdown intensity with

slight extrapolation from the results of Morgan in 1975. [27] It should be noted that the SRS limit in table 1 for the SRS fiber lasers would scale significantly higher with a shorter fiber due to the intensity conversion to the 2nd order Stokes starting after fully converting to the 1st order Stokes, while the gain for the other two is independent of the SRS limit. For instance, a 1 m HCPCF with 580 psi N_2 has an SRS limit of 45 kW with same assumptions except the length. Thermal mode instability and thermal lensing were not included into table 1 due to a lack of information regarding these effects in inhibited-coupling HCPCFs. These improvements come from the low mode overlap with the silica and the high threshold intensities for them in gases. The gain from solid core fibers comes from the dopants energy levels trapped in the silica lattice, such as holmium, erbium, neodymium and thulium. The gain in gas-filled HCPCFs comes from the gas trapped inside the fiber core, such as nitrogen, hydrogen, acetylene, methane, nitrous oxide, and iodine. [10, 9, 28, 16, 8] HC-PCFs have several added complications such as filling the gas and guiding the light without TIR. TIR is not possible due to the gas's index of refraction being lower than silica; in order to maintain the guiding properties, one of two guiding mechanisms can be used, photonic band gap or inhibited-coupling. The details of the photonic band gap guiding mechanism are beyond the scope of this report, but they rely on a periodic interior structure which acts like a Bragg grating allowing guidance even with an air core. Inhibited coupling works due to a "strong transverse mode mismatch" between the modes of the core air-mode and the cladding modes. [7] The benefit of inhibited coupling guiding is the weak overlap with the core mode in the clad, which limits mid-wave infrared absorption in silica cladding. It requires higher-order modes to be sufficiently leaky in order to maintain single mode operation, and the lowest loss in an inhibited coupling HC-PCFs is limited by surface roughness scattering at 0.65 dB/km, which is still worse than telecommunications solid-core fibers with losses of

between 0.2 dB/km and 0.3 dB/km in the C- and L-bands from 1530 nm to 1625 nm. [29, 30] In the case of a Raman laser, the SRS limit for maximum scaling is determined by the transition into higher-order Stokes transitions and will lower with increasing pressure due to the increasing gain. The geometry of the fiber plays a large role in the wavelengths that are transmitted, which is the limiting factor for wavelength selection in current gas-filled HC-PCFs. Design parameters have been studied for getting specific wavelengths, but a different fiber is currently needed for different ranges of wavelengths. HCPCFs can be found between UV at 218 nm and telecommunication wavelengths, between 2 μm and 3 μm, at the CO laser line at 5.5 μm, and at the CO_2 line at 10 μm with the last two made from chalcogenides instead of silica. [31, 32] HC-PCFs with low loss designs have very good transmission profiles for specific systems as long as the desired input and output wavelength ranges are known.

Table 1. Comparison of approximate critical CW powers/intensities for limiting processes in solid-core, HOFGLAS, 580 psi N_2 and 1,160 psi N_2SRS HCPCFs. The gas-filled HCPCFs has higher critical powers due to its low optical overlap with the silica and gas-phase materials having significantly higher thresholds for these processes due to a low index of refraction. Calculations were based on a 40 μm core diameter in 10 m fiber at 1.5 μm. The SRS limit to the SRS laser is defined as 50% of the 1st Stokes line converted into 2nd order Stokes line, which means a shorter fiber would allow a higher limit while not limiting max lasing power.

Limiting factor	Solid core	HOFGLAS (5 torr)	580 psi SRS	1160 psi SRS
SBS	1.3 kW	10 MW	1 MW	500 kW
SRS	30 kW	600 MW	5 kW	3 kW
Material damage	8 kW	120 kW	57 MW	38 MW

2.3 Previous Work

Raman in a Gas Cell.

In order to determine the gain at different number densities, the linewidth of the transition must be understood. The Q branch of the stimulated Raman process of

molecular nitrogen at densities up to 800 amg was explored Lavorel et al. [2] The desire to remotely investigate very high pressure environments spectroscopically like near combustion of rockets drove this work. Lavorel et al pumped the nitrogen with a 12 ns 10 Hz pulsed frequency doubled ND:YAG laser with a 500 kW peak power and probed with frequency stabilized CW argon ion laser at 500 mW. The number densities ranged from 135 amg to 800 amg. The cell was made from a beryllium-copper alloy with sapphire windows in order to withstand the significant pressure differential. There is initially a red shift and narrowing with increased density until around 500 amg. Afterwords, the SRS begins blue shifting but continues narrowing until around 700 amg where it begins broadening. The linewidth is quasi-Lorentzian from 280 amg to 700 amg, where the vibrational broadening coefficient becomes non-negligible. The narrowing is fairly well described by perturbation theory which gives a rotational relaxation constant. Lavorel et al described several fitting models for fitting the HWHM with varying success. Models were good at lower densities or at higher densities but not both.

High efficiency N_2 Raman lasing was explored by Zhang et al. [33] They used a pulsed 10 ns 10-Hz Nd:YAG laser to pump a 2 m cavity of 1:1 N_2 and separately O_2 with He at total pressures up to 1000 psi. A fraction of the pump laser was used to excite a dye laser for seeding at 581 nm or 607 nm for the nitrogen or oxygen, respectively. The conversion efficiencies reported were the average over 100 pulses with corrections for prism reflection and window absorption losses in their system. Without a seed, N_2 had a max conversion efficiency of 19%, which improved to 35% with the dye laser seed. O_2 went from 9% with out a seed to 21% with a seed. However, the oxygen had a higher percentage converted to the second Stokes line (14% vs 2%), which was most likely due to the larger Raman shift of nitrogen.

Komine et al. explored converting into higher Stokes orders by pumping hydrogen

at 355 nm and observing first and second Stokes orders. [34] Brillouin scattering limited input energies of pulses in earlier liquid phase Raman shifts. Molecular gases however are much more robust against significant Brillouin scattering. In steady state, the nth Stokes order amplification is described as

$$\frac{dI_n}{dz} = g_{n-1} I_n I_{n-1} - g_{n+1} I_n I_{n+1}, \tag{12}$$

where the I_n is the intensity of the nth Stokes line and $g_{n\pm1}$ is the gain covert up for down. Four Stokes lines were seen from the pulsed UV source at 416 nm, 503 nm, 636 nm, and 864 nm. Seeding of the amplifier was obtained via a resonator cavity of H_2 with filters chosen to pass only desired stokes lines. Unstable resonators were used to show increased conversion efficiency into higher order Stokes lines.

For molecular nitrogen, Averbakh et al was the first to demonstrate SRS and for both vibrational and rotational stokes transitions. [21] It was pumped with 300 MW peak power in 1 ns pulse from a second harmonic neodymium laser at 532 nm. The most prevalent rotational transitions were from the J=8 and 10 levels to the J = 10 and 12 levels due to nitrogen Raman having only even J transitions due to odd J being forbidden transitions and the temperature determining the populations following a Boltzman distribution, which is unstated in the paper. In order to show the rotational Stokes lines the pump needed to be circularly polarized. The threshold for vibrational SRS at pressures under 5 atm was on the order of GW/cm^2 with the rotational SRS having a lower nearly constant threshold until the two cross at around 3 atm where the rotational transitions become suppressed by the vibrational transitions. Averbakh focuses significant portions of his paper discussing this effect, but for the purpose of this work it is sufficient to note that the pressures used will only be minorly affected by rotational SRS if at all.

HC-PCF Gas Lasers.

An HOFGLAS inhibited-coupling negative curvature Kagome-structured HC-PCF filled with iodine and pumped at 532 nm was demonstrated in 2015. [28] The absorption cross-section was reported at around 10^{-16} cm^2 in the visible spectrum. 300 mTorr in a 20-cm HC-PCF was used for the CW emission between 1200 and 1350 nm. The fiber loss of the lasing frequency was measured to 30 dB/km prior to cleaving the 20-cm fiber for use. Kagome-structured core to cladding resonances result in high transmission losses at peaks whose positions are well described by Nampoothiri et al. The pump threshold was at 7 mW,or an intensity of 290 W/cm^2, and a maximum slope efficiency of 4%. The authors expect improvements on slope efficiency with the addition of a buffer gas due to spin orbit relaxation.

Recently, a 80 Torr nitrous oxide-filled 45 cm long 85 μm core diameter HC-PCF pumped at 1.517 μm was demonstrated at 4.6 μm with a 3% slope efficiency from a mirror-less laser cavity. [9] Inhibited coupling HC-PCFs offer optical overlaps, which are generally lower than guiding via photonic band gap designs. The effective loss of this HCPCF was described by confinement loss and silica absorption. The resulting loss was 33.6 dB/m, approximately one fifth of the gain of the system, and the coupling efficiency was only about 45%. Given all these parameters, the threshold pump pulse energy was 150 nJ. The 4.6 μm emission was the second overtone with an absorption cross section of 10^{-20} cm^2. The gain of the overtone is the absorption cross section times the top state. The top state in time is described as

$$N_3(t) = \left(\frac{\sigma_{13} N_1}{h\nu_p}\right) I_p \tau_3 (1 - e^{-t/\tau_3}), \tag{13}$$

where σ_{13} is the absorption cross section from the ground to the top state, τ_3 is the time constant for leaving the top state (inversely to pressure by rotational relaxation),

ν_p is the pump frequency, and I_p is the pump intensity. The experiment resulted in a gain of 0.9 cm^{-1}.

A pulsed hydrogen SRS laser was demonstrated with a 532 nm, 6 ns, 20 Hz pulsed pump with a 0.8 $\pm$ 0.2 μJ vibrational Stokes threshold and 3.4 $\pm$ 0.7 μJ vibrational Anti-Stokes threshold in 2002. [16] A photonic band gap fiber was used due to it being before the modern inhibited-coupling HC-PCFs options. Two gas cells were connected by the fiber with a pressure of 246 psi of H_2 with a similar design as the work proposed here. Benabid et al go into significant detail about the fabrication of the fiber for those interested. For instance, the photonic band gap was formed from stacking capillaries to fill the core with the seven capillaries in the middle empty to form the waveguide. A cut-back study of the fiber was performed which demonstrated 30 cm led to optimal conversion of 20% into the first Stokes line and just under 1% in the first Anti-Stokes line.

The first CW hydrogen Raman HC-PCF laser was demonstrated with a 30 m fiber in 2007. [11] The laser had a 2.25 W threshold in a mirror-less or single-pass configuration and a 600 mW threshold with the addition of fiber Bragg gratings spliced onto each side of the fiber. A 1064 nm fiber laser was used as the pump. It was a purely rotational Raman laser, which provided significant advantages in terms of a low quantum defect with an output at 1135 nm. The conversion efficiency peaked at 14.5 psi with 99.9% of the output light being converted to the rotational Stokes line and dropped with increased pressure. The threshold dropped with increasing pressure up to 145 psi where it leveled off.

A stimulated vibrational hydrogen Raman HC-PCF has likewise been demonstrated with a 1064 nm pump. [4] The rotational Raman needed to be suppressed in the 6.5 m fiber, which was achieved by linearly polarizing the pump light, using a short fiber, and filling the fiber with higher pressure hydrogen (23 bar at peak

conversion efficiency). The power threshold of the CW case is described by

$$P_{th} = G_{th} * A_{eff}/(\gamma_g l_{eff}), \tag{14}$$

where γ_g is the steady-state Raman gain coefficient, l_{eff} is the effective fiber length, A_{eff} is the fibers mode field area, and G_{th} is the threshold net gain. l_{eff} can be found using, $l_{eff} = (1 - e^{l\alpha})/\alpha$, where l is the length of the fiber and α is the attenuation of the fiber at the pump wavelength. A 0.7 ns pulse with a 7.25 kHz repetition rate giving a 65 mW average power was used. Despite the pulsed pump, a steady-state SRS model was used fairly accurately with accurate predictions for both the vibrational and rotational SRS as a function fiber length; however, the pump had higher than predicted residuals in all lasing cases. The approximations were justified due to three factors: the negligible walk-off effect in a fiber less than a few hundred meters in the length, the dephasing time for the hydrogen was much shorter than the pump duration at the high pressures used, and other Stokes intensities were negligible. These approximations left three differential equations

$$\frac{d}{dz} I_{Sv} = (\gamma_{Sv} I_P - \alpha_{Sv}) I_{Sv} \tag{15}$$

$$\frac{d}{dz} I_{Sr} = (\gamma_{Sr} I_P - \alpha_{Sr}) I_{Sr} \tag{16}$$

$$\frac{d}{dz} I_P = (-\gamma_{Sv} I_{Sv} - \gamma_{Sr} I_{Sr} - \alpha_P) I_P, \tag{17}$$

where I_{Sv} is the vibrational Stokes intensity, I_{Sr} is the rotational Stokes intensity, I_P is the pump intensity, γ_{Sv} is the vibrational gain coefficient, γ_{Sr} is the rotational gain coefficient, α_{Sv} is the fiber absorption per meter at the wavelength of the vibrational line, α_{Sr} is the fiber absorption per meter at the wavelength of the rotational line, and α_{Sp} is the fiber absorption per meter at the wavelength of the pump. An optical-to-optical efficiency of 28% was measured for coupled light to the vibrational Stokes line

at 1907 nm. The output shows the vibrational Anti-Stokes as well as slight rotational first-order Stokes and Anti-Stokes lines, but the rotational Stokes orders are not truly resolvable from the pump due to the small shift and some combination of instrument lineshape along with the lineshapes of the rotational line and pump.

Gladyshev et al showed improvement on the H_2 HC-PCF pumped at 1064 nm by improving the conversion efficiency from 50% to 87% of the quantum efficiency, 55%. [35] The improvements stem from fiber design changes in the form of a ring of conjoined circular capillaries for the inhibited-coupling, which reduced losses compared to Wang et al's conjoined cone ring structure. As with the previous works, the fiber was hermetically sealed into two small chambers on each end and had no other tubing connecting the two chambers. They achieved average powers of up to 300 mW Raman output with their 125 ns pulsed pump with an average power of 1 W through a 2.25 m fiber. They observed the first four orders of Anti-Stokes from the hydrogen leaking laterally out of the fiber due to it not guiding those wavelengths at 456 psi. The output showed strong first-order Stokes as well as the first two orders of anti-stokes when linearly polarized, which is likely due to the much lower losses in their fiber at the shorter wavelengths. When circularly polarized, they observed the rotational stokes order off of each of the previously mentioned vibrational stokes orders.

Higher order Stokes lasing has been demonstrated in HC-PCFs. For example, a 1064.6 nm pumped methane-filled HC-PCF lased at 1543.9nm and 2800nm in a 2 HC-PCF setup. [19] The pump was telescoped into the first HC-PCF then that output is telescoped into a second HC-PCF with different internal structure. The resulting laser system had a quantum efficiency of 25% and maximum output power of 13.8 mW at 160 psi of methane in the second stage. Higher pressures lead to too much power coupling into higher order Stokes lines, which had high losses in the fiber

structure used. The Raman threshold is inversely proportional to gas pressure, as expected.

III. Experimental Setup

In this chapter, the experimental setup for the scattering experiment, 2-mirror cavity experiment, and HCPCF experiment will be described. The scattering experiment sent the pump light through the chamber in a single pass configuration and observes the scattering as the pressure in the chamber changes with two cameras. The 2-mirror cavity experiment pumps into the same chamber but into two highly reflective mirrors and scales the pressure. The HCPCF experiment utilizes Polyetheretherketone (PEEK) tubing to connect two chambers and hold the fiber length, which allows for pressure scaling without concern for the HCPCF bursting. A McMaster-Carr 3196K871 pressure transducer was used for measuring the pressure in all experiments.

3.1 Scattering Setup

The experiment setup for the spontaneous Raman and Rayleigh scattering is seen in Fig. 4. The chamber had one gas connection and a blow off connection rated for 4,000 psi, the chamber's rating for pressure. A Verdi V-18 532 nm pump is sent into a 14" 304 stainless steel chamber with Rayotek 4" national pipe tapered (NPT) fitting Sapphire windows chosen due to its high transmission profile over the visible and infrared spectrum and tolerance for high pressures. The pump produced a 16.5 W beam with a M^2 of < 1.1 and a $1/e^2$ beam diameter of 2 mm. The beam is steered via two Thorlabs BB1-E02 mirrors, and a Thorlabs IO-5-532-HP 532 nm Optical Isolator is used to prevent back reflections from damaging or reducing the stability of the pump system. The Sapphire windows are 80±2% transmissive at both wavelengths, but the beam is sent through at an angle to the windows such that no resonate behavior is established. A FLIR Grasshopper 3 GS3-U3-89S6M-C

camera is placed on each side of the chamber, which views the beam at between 13 and 16 degrees off the horizontal axis through a 25 mm lens on output side and 15 mm lens on the input side. This allowed for the characterization of the forward and back scatter of the beam as a function of N_2 pressure. The temperature was held relatively constant due to slow fill rates of around 1 psi per second; thus, the number density increased linearly with the pressure, which was measured in 1 minute intervals. The camera's record images at the same 1 minute interval, so that the pressure and scattering were known together at each instance. The chamber was first brought to a rough vacuum of less than 1 psi in order to get a reference frame. The reference frame was used in background subtracting away from future frames the noise from pump scattering and reflections at the windows and the rest of the non-chamber system, which was assumed to be constant over the test. After collecting at least two vacuum frames, the chamber was slowly brought to 3,000 psi with stops at each 500 psi interval for at least 1 additional frame to determine consistency of the measurements post test. The pressure was not maintained at any pressure for more than a few minutes due to a small leak at the window due to chamber NPT connection, which was unable to be completely sealed. The following techniques were used to seal the windows: Polytetrafluoroethylene (PTFE) tape wrapped from 3 to 8 layers thick and at widths of 1/4" and 1", Permatex 80633 with and without PTFE tape, Anti-Seize Technology TFE with and without PTFE tape, Loctite 565 with and without the primer for steel applications, Loctite 565 on the male end of the NPT fitting wrapped in PTFE tape, and Loctite 565 on both sides of the NPT connection with PTFE tape in between. All products listed other than the PTFE tape were pastes of varying viscosity. The window was tightened initially to the rated 400 ft-lb with a six foot torque wrench, but the torque was increased to 600 ft-lb after talking with Rayotek due to a lack of sealing. For pressures up to 1800 psi, PTFE tape

could limit leaking to approximately 0.33 psi/min. After that, the best method was Loctite 565 on both sides of the connection with PTFE tape in between but was not consistent with leak rates between 40 psi/min to 240 psi/min. For the Raman scattering, a long pass 600 nm chromatic filter was placed in front of each camera which adequately filtered out any 532 nm light. There was an additional source in this range at 680 nm likely from titanium impurities in the sapphire windows, which upon visual inspection and investigation of the data did not scale with pressure and was taken out with the previously mentioned background subtraction. For the Rayleigh scattering, a short pass 550 nm chromatic filter was placed in front of each camera along with a ND filter to prevent saturation of the cameras.

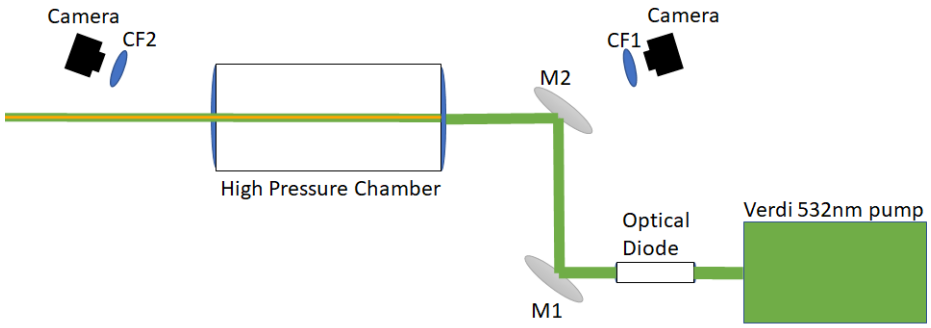

Figure 4. Green pump light is sent through the cavity via 2 steering mirrors (M_1 and M_2) where light interacts with the high pressure nitrogen gas which continues into a beam dump. The cameras each have a chromatic short pass, 550 nm, or long pass, 600 nm, filter (CF_1 and CF_2) to record the Rayleigh or vibrational Raman scattering.

3.2 Two-Mirror Cavity Setup

Using the same chamber, a two mirror cavity was added with a variable separation with a 12 cm screw through the base as seen in Fig. 5. The input coupler mirror was a Newport 10CV00SR.30F with a effective focal length of .5 m and reflectivities of 95.5% at 532 nm and $>$ 99.97% at 607 nm. The output coupler was a flat Newport

10CM00SB.1 with reflectivity of $> 99.9\%$ for both wavelengths. The mirrors were mounted to Newport ultra-high vacuum picomotor mounts for alignment of the cavity at pressure without opening the chamber with wires connected through a 1" NPT feed thru, Douglas Electric 5368-16-0. While they are not rated for use at high pressure, they functioned even up to 3,500 psi. The design of the mounts for use at ultra-high vacuum pressures allowed their use at high pressures. The cavity was setup with mirror spacings of 12 cm, 10 cm, and 4 cm. The 4 cm cavity length was used to mitigate two issues, one after noting significant Rayleigh scattering from the high pressure and the other was because of a chamber leak that seemed to cause cavity stability issues. This effort is further discussed in the results section. Alignment for the cavity was initially performed at atmospheric pressure. This was done by aligning the input beam parallel to the table with the two steering mirrors while hitting the center of the input coupler, then steering the strong back reflection to the output of the optical isolator. This will have made the center of the input coupler perpendicular to the pump light. A faint spot in the back reflection was used to get the output coupler roughly aligned the same as the input coupler. When fully aligned, a pristine spot was present out of the output coupler even at the minimum input power of 10 mW. Tweaks were made if the cavity needed slight realignment as pressure increased. However, significant pump light exits the back sapphire window from back reflections and expansion off the input coupler and window, which is most prominent on the open edge side of the mounts. The input coupler and mount in the chamber can be seen in Fig. reffig:CavityPic. This experiment was pumped with powers up to 18 W from the Verdi. The cavity test was never run after pulling a rough vacuum due to there being no need to background subtract a camera image.

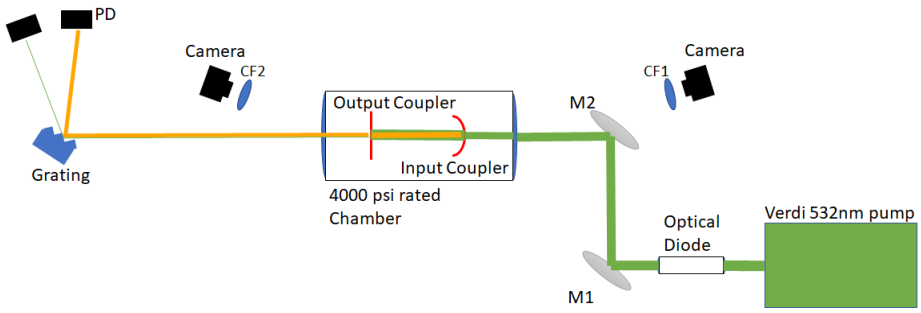

Figure 5. Green pump light is sent into the cavity via 2 steering mirrors(M_1 and M_2) where the light resonates in the high pressure nitrogen environment which outputs into a diffraction grating that splits the pump and 1st order Stokes beam. The cameras remained from the scattering experiment, the data showed the low intensity of the output producing negligible scattering and the input coupler back reflections causing significant noise, which limited the value of the data.

3.3 Hollow-core Photonic Crystal Fiber Setup

Two shorter chambers were used for the HCPCF experiment with each having a 4" NPT fitting sapphire window as seen in Fig. 7. The chambers were connected by Zeus Inc. made polyether ether ketone, PEEK, tubing with a 1/4" outer diameter and 1/8"' inner diameter which can handle the pressures required while allowing the HCPCF to easily fit inside. Only the output chamber had a Swagelok gas connection and a Fike over pressure rupture disk connection. The 75 mm lens, L_1, was chosen based on the equation for coupling in to a single-mode fiber

$$f = \pi D\omega/4\lambda, \tag{18}$$

where D is the $1/e^2$ beam waist, ω is the mode field diameter, and λ is the wavelength being coupled into the fiber. This equation is the same used for single mode solid-core fibers due to both using a Gaussian mode-matching scheme as opposed to TIR, which will not work in HCPCFs as previously discussed in section 2.2. The pump beam waist is 2 mm where the lens is placed, and the fiber has a mode field diameter

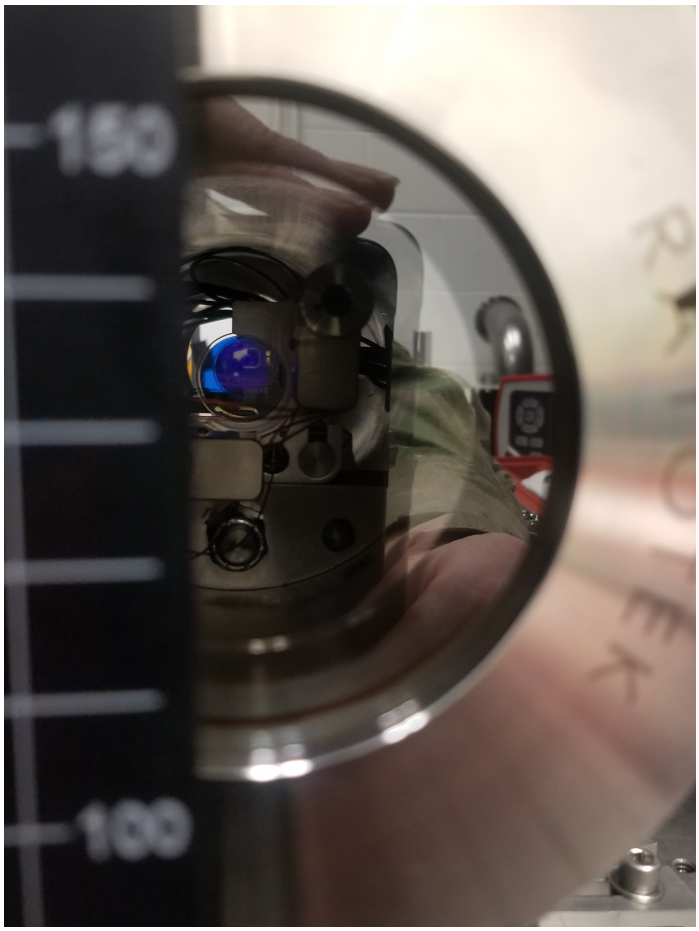

Figure 6. Displays the input mirror in the mount with the top left open faced. The ruler on the left is in millimeters.

of 24 ± 1 μm. In the case used, eq. 18 worked out to 71 mm, and the closest available lens was 75 mm. The HCPCF used was a GloPhotonics PMC-C-Green with excellent transmission for visible wavelengths with losses less than 100 dB/km between 500 and 700 nm as seen in Fig. 8. More specifically, the loss is rated to be 30 ± 10 dB/km at 532 nm. The beam was initially coupled with low input power and at atmospheric pressure but needed to be adjusted as power increased due to beam drift with changing pump powers and as pressure changed due to the fiber moving from the gas flow. A better method for fiber stability would have been a significant improvement on the current setup, which was held by a magnetic v-groove mount with approximately an

inch hanging past the front of the mount. The experiment consisted of pressures ranging from atmospheric pressure, < 1 psi to 1500 psi to determine how the 532 nm and 607 nm powers changed under these conditions.

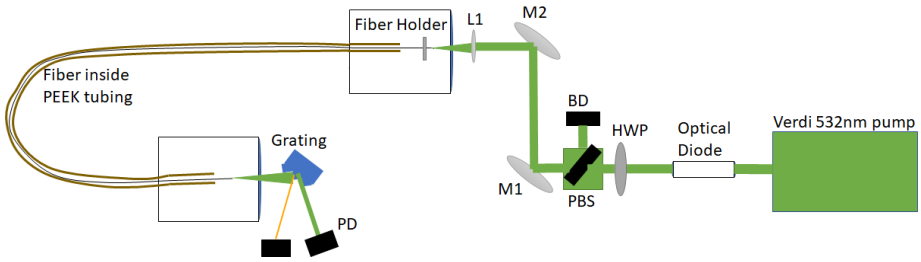

Figure 7. Green Pump light is coupled into the HC-PCF via a half-wave plate(HWP), polarization beam splitter (PBS), 2 steering mirrors(M_1 and M_2) and an 75 mm focal length lens which outputs into a diffraction grating that splits the Pump and 1st order Stokes beam. The fiber sits inside PEEK tubing, which is connected to the chambers with a 1/4" Swagelok connection. Inside the input coupling chamber, the fiber is held in a v-grove magnetic mount for increased stability when coupling.

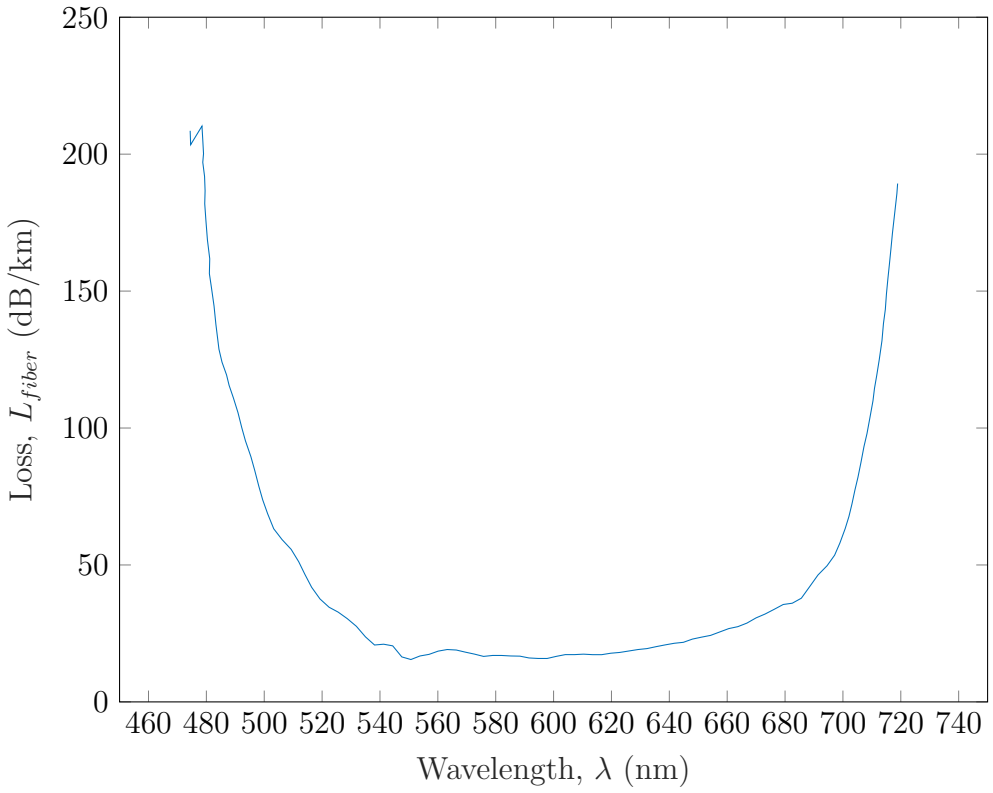

Figure 8. Loss according to the specifications of the Glophotonic PMC-C-Green HCPCF used in the experiment. It shows the large low loss window for testing any of N_2, O_2, or H_2.

IV. Experimental Results

4.1 Scattering Experiment

The scattering test shows two distinct characteristics for the design of a CW SRS laser. First, the eventual lasing seed of spontaneous Raman scattering which can readily be observed by placing a high-pass filter in front of the two cameras discussed in the experimental setup section. The second is a loss parameter for the nitrogen SRS laser, Rayleigh scattering, which can be separated with a low-pass filter and slight off-axis viewing angle of the beam.

The spontaneous Raman scattering resulted in the expected linear scaling with number density in both the forward and backwards arc seen in the Fig. 9 and Fig. 10. Several images of the scattering after image cleaning can be found in Apdx. A. One of the prominent features of the images was bright red scattering through the the sapphire windows that most likely points to titanium impurities in the crystal. This was removed from the data by subtracting a rough vacuum pressure frame from all of the frames, which should be adequate due to their being minimal effects inside the sapphire window with increased chamber pressure and the window remains dark in all of the images except minor portions peaking out at the windows from beam drift. It is important to remember while the SRS gain is expected to go up at an exponential rate with pressure, the spontaneous Raman is a function of the differential Raman cross section and the number density. The forward scattering camera appeared to be collecting darker images even before the filter was placed in front of it, so the data being lower is not necessarily a reason to assume there is a preference for back scattering.

The Rayleigh scattering cross-section is four orders of magnitude higher than the spontaneous Raman cross-section, so neutral density (ND) filters were placed in front

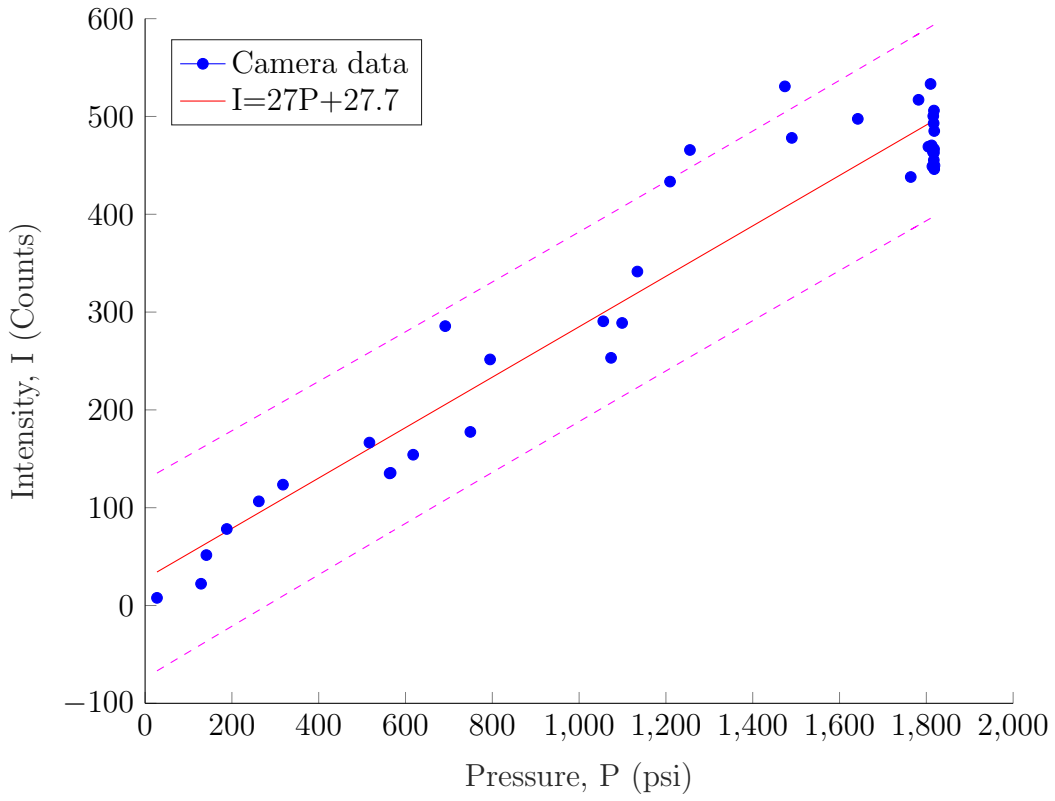

Figure 9. Shows the linear scaling of the Raman scattering in the forward arc estimated as 0.21 to 0.28 radians for the beam with scaling pressures that where limited by a significant gas leak at the chamber's window. It reflects the average value of the entire beam in the frame in the image to limit noise with measurements taken in 1 min intervals plotted with x's. The counts are lower at all points for the forward scatter due in part to the difference in cameras. The camera had a high pass 550 nm filter, and the data used a rough vacuum frame as a background to subtract away non-pressure dependent light sources.

of the camera's to prevent saturation. It should have an angular dependence, which was unable to be strongly shown from the limited viewing angle collected. Comparison with a camera orthogonal to the chamber would have allowed a more definitive result for this type of measurement. To limit noise in the data, an average of the full beam in view was used in Fig. 11 and Fig. 12. The data showed again a strong linear relationship particularly in the back scatter camera, which had an ND 1 filter. The forward scattering camera had an ND 2 which appears to have resulted in a number of the low pressure measurements falling in the noise floor and noiser results thereafter.

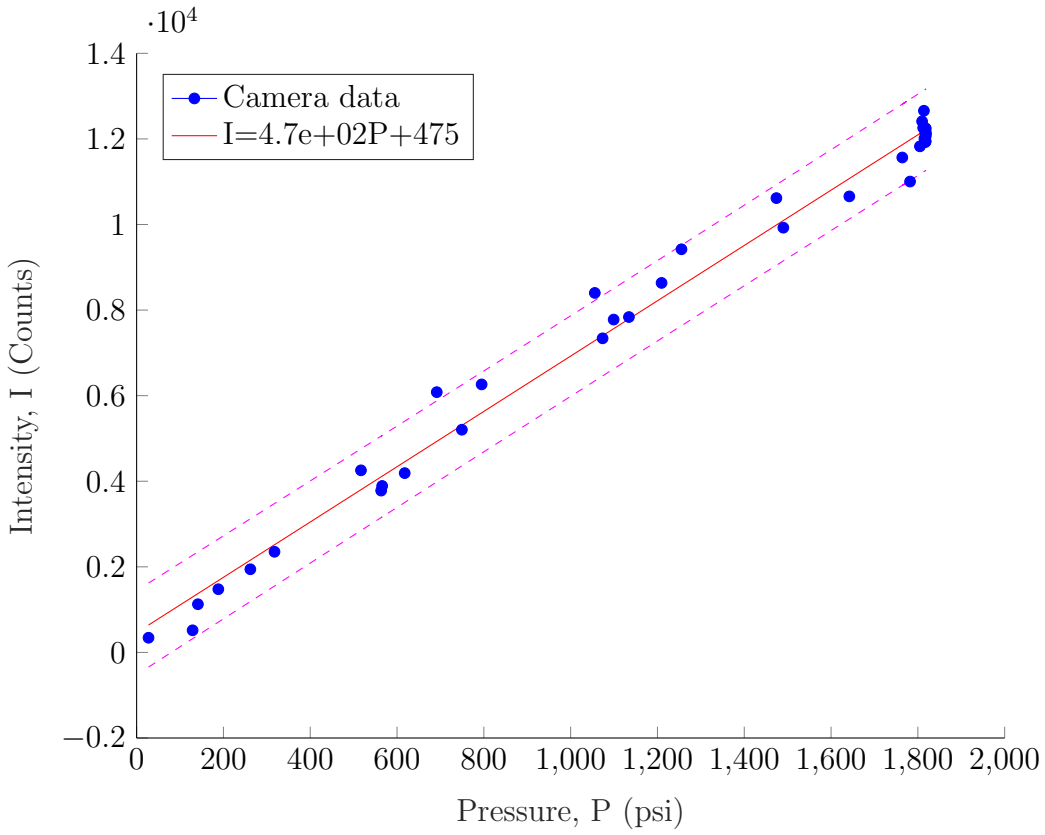

Figure 10. Shows the linear scaling of the Raman scattering in the backward arc estimated as 0.21 to 0.28 radians for the beam with scaling pressures that where limited by a significant gas leak at the chamber's window. It reflects the average value of the entire beam in the frame in the image to limit noise with measurements taken in 1 min intervals plotted with x's. The camera had a high pass 550 nm filter, and the data used a rough vacuum frame as a background to subtract away non-pressure dependent light sources.

As with the Raman scattering, several images of the scattering after image cleaning can be found in Apdx. A.

4.2 Two-Mirror Raman Cavity

The cavity experiment gave results counter to what would be expected from the equations found section 2.1. Despite eq. 9 pointing to lasing prior to 18 W by 3000 psi in the 10 cm cavity, no lasing was seen even up to 3800 psi. The cavity instead showed increasingly bright green filling the entire cavity. It also showed orange, likely

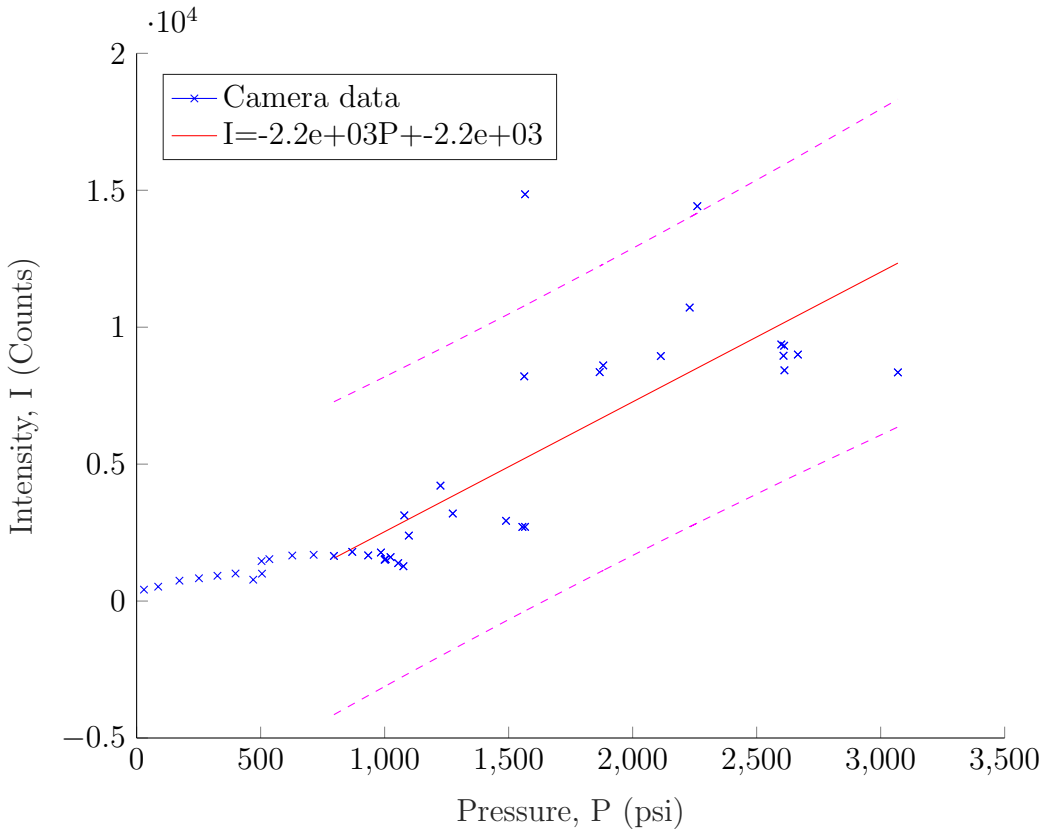

Figure 11. Shows the linear scaling of the Rayleigh scattering in the forward arc estimated as 0.21 to 0.28 radians for the beam with scaling pressures that where limited by a significant gas leak at the chamber's window. It reflects the average value of the entire beam in the frame in the image to limit noise with measurements taken in 1 min intervals plotted with x's.The camera had a ND 2 absorptive filter after the low pass 550 nm filter due to saturation of the camera, and the data used a rough vacuum frame as a background to eliminate pressure independent light sources. The ND 2 filter resulted in many frames in the noise floor at the early pressures and more variation from particularly noisy frames as seen in plotted raw data.

607 nm from the vibrational Stokes shift due to no other known source, increasingly throughout the cavity. Attempts to measure the wavelength of the orange were unsuccessful using an Ocean Optics QE Pro spectrometer presumably due to the signal being below the noise floor. It must have been either all spontaneous Raman scattering not maintained in cavity or Rayleigh scattering of the orange beam along with spontaneous scattering. The orange on the input coupler side can be seen in Fig. 13. The other qualitative result was that the leak that present in the chamber caused

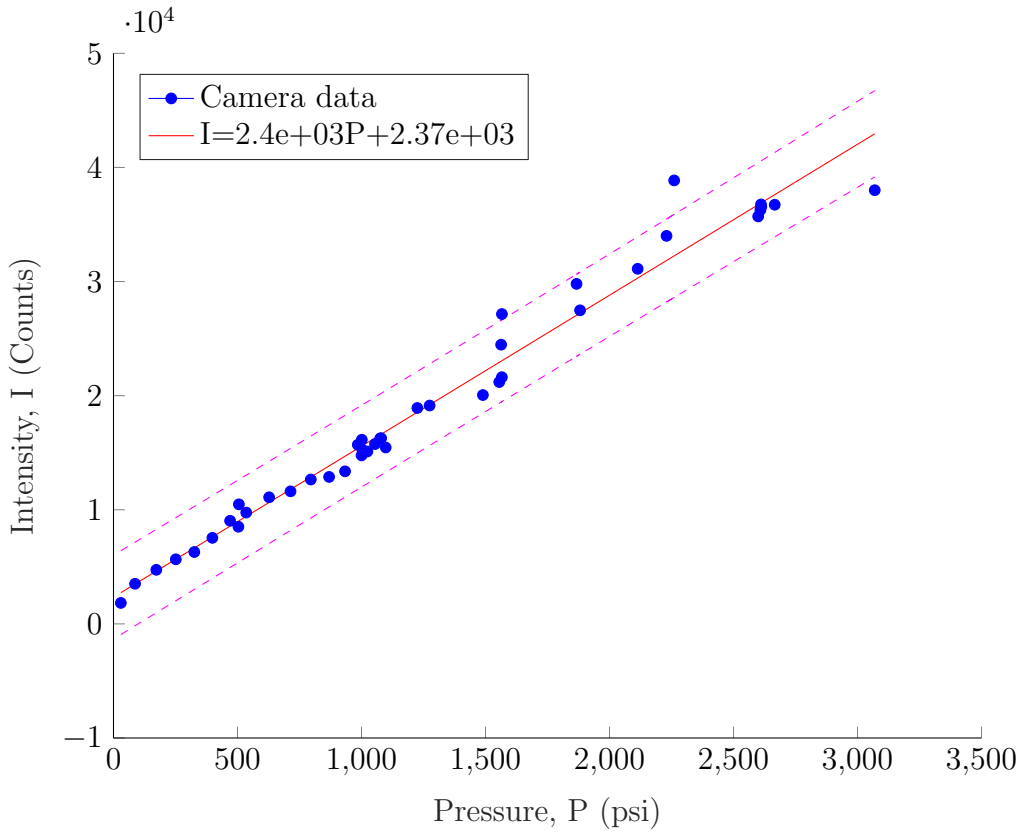

Figure 12. Shows the linear scaling of the Rayleigh scattering in the backward arc estimated as 0.21 to 0.28 radians for the beam with scaling pressures that where limited by a significant gas leak at the chamber's window. It reflects the average value of the entire beam in the frame in the image to limit noise with measurements taken in 1 min intervals plotted with x's.The camera had a ND 1 absorptive filter after the low pass 550 nm filter due to saturation of the camera, and the data used a rough vacuum frame as a background to subtract away non-pressure dependent light sources.

the beam to drift, which was more prevalent with larger leaks or when filling at at higher flow rates. It caused the beam in the cavity to lose its resonant nature, which was seen as the output green spot splitting into two moving weak spots that would brighten up when overlapped for short portions. Due to Rayleigh scattering only linearly scaling with intensity and SRS scaling with intensity squared, the chamber was shortened to 4 cm. The equations as previously stated would still point to lasing at this point, but there was no orange beam out of the output coupler. These two together point to a need for an update to the model. Due to the intensity not being

high enough, the two solutions with the same pump are to use shorter focal length mirrors which would limit gain volume but increase beam area as seen from eq. 6 and eq. 7 or move to an HC-PCF.

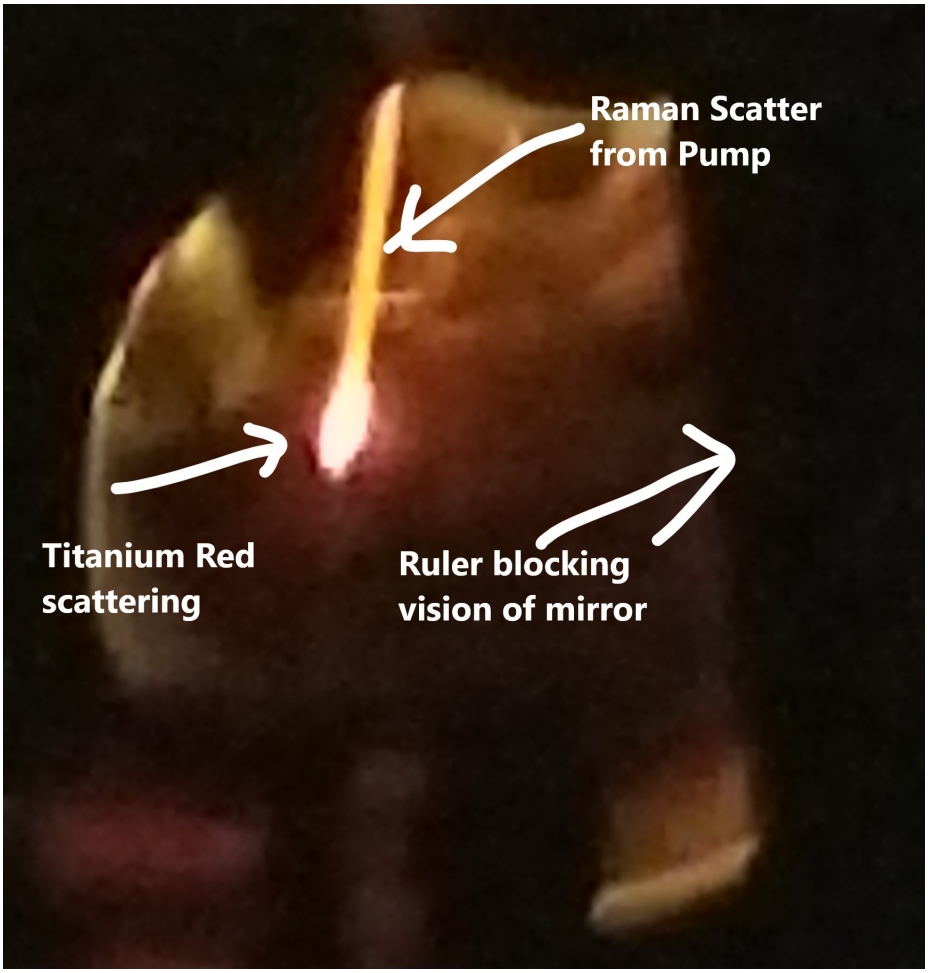

Figure 13. Displays the scattering above 550 nm in a color format prior to entering the cavity. The bright spot is a deep red and likely from the titanium impurity and was too bright for the phone camera used to take the picture. The orange beam is likely Raman scattering from the 532 nm input beam.

4.3 Hollow-core Fiber

The HC-PCF experiment suffered from chamber leaking like the other two experiments, scaling with pressure from 0.33 psi/min near atmospheric pressure to 90

psi/min near 3000 psi. This resulted in the fiber end moving even when held by the V-groove mount, which made coupling extremely difficult at low pressures and impossible at high pressures with the larger leak rate. A coupling efficiency of $56.72 \pm 0.35\%$ at atmospheric pressure was achieved. This was calculated from an input of 392 ± 1 mW, 80% transmission through each window, 90% transmission through each lens, 98% transmission through the fiber assuming the 30 dB/km from the specifications and 3 m, and 112.9 ± 0.4 mW. Coupling with the leak was limited to nearly 51% at pressures below 400 psi, while no consistent coupling was achieved at higher pressures. At atmospheric pressure, the divergence half-angle was measured at 3.5° as calculated from Fig. 14. An image of the multi mode spot at maximum coupling efficiency is seen in Fig. 15. All of the measurements were measured far past the Rayleigh length of 0.8 mm, defined by $z_0 = \pi * \omega_0^2/\lambda$, which means that the expansion should be at nearly a constant angle. The diffraction limit for the beam was 0.81°, based on $\Theta = \lambda/\pi\omega_0$. This means that the beam was certainly not single fundamental mode operation. When aligning, the mode structure changed with the focus location from the lens. However, it was never Gaussian in appearance and always had a similar spot size at a fixed distance. Similar coupling efficiencies were achieved with an 88 mm lens that showed similar multi-mode behavior.

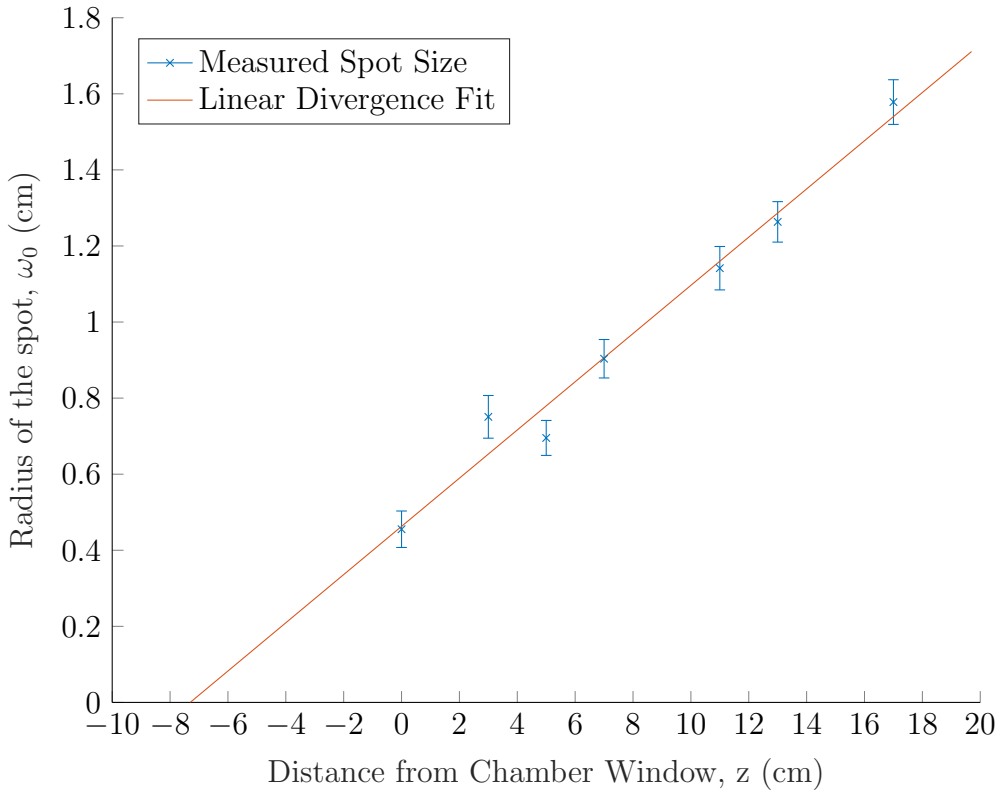

Figure 14. Shows how the beam expanded after the window. The error is based on ±2 pixels on either side for determining beam diameter. It was used to calculate the divergence of the beam.

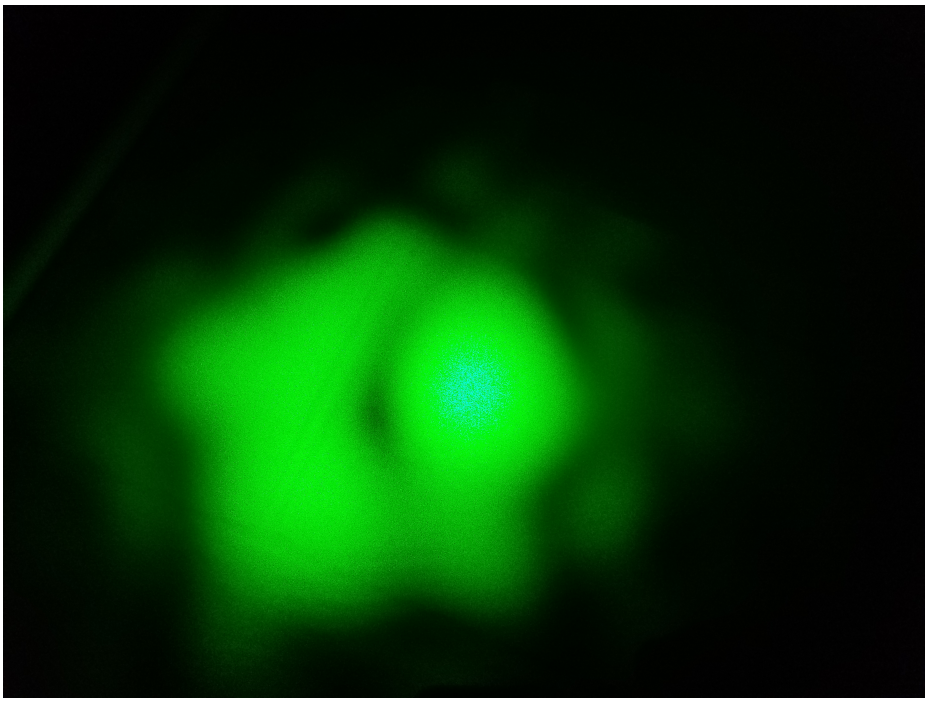

Figure 15. Displays the multi mode far field structure on a wall when coupled into the HCPCF at 57% efficiency.

V. Model

Given the results of the two-mirror cavity and HCPCF experiments, it is clear that the equations for each need modification for the high pressures used for SRS in N_2. The significant Rayleigh scattering present in the cavity experiment are the most influential to both sets of equations. The other needed addition is the mechanism for adding the first Stokes field energy into the HCPCF model. These together provide a substantial improvement for the design of a CW N_2 SRS laser.

5.1 Two-Mirror Raman Cavity

The initial model for the two-mirror cavity was developed in eq. 9, eq. 10, and eq. 11. The expected results for these in the 10 cm setup is shown in Fig. 16, which assumed that Rayleigh scattering was not a significant source of loss. However at the pressures considered here, Rayleigh scattering is on the order of the mirror cavity losses. If instead, the Rayleigh scattering loss per second, scattering per meter multiplied by the speed of light, is included then the threshold changes as seen in Fig. 17. The stimulated Raman gain should go up linearly with intensity. Shrinking the cavity will reduce the spot size and increase the intensity, but as Fig. 18 shows the smaller cavity does not overcome the combination of loss mechanisms. The increased mirror losses result in worse performance over all given the pump and mirrors used. The simpler model does get closer to the updated model in this case because the mirror losses are becoming more dominant compared to the Rayleigh losses.

The Rayleigh losses are based on the scattering cross-sections found in Shardanand and Rao's report for nitrogen, though the authors include several other gas including hydrogen and oxygen. [36] The Rayleigh cross-section was assumed to scale with $1/\lambda^4$; though, it does vary slightly from this as the index of refraction also has an effect

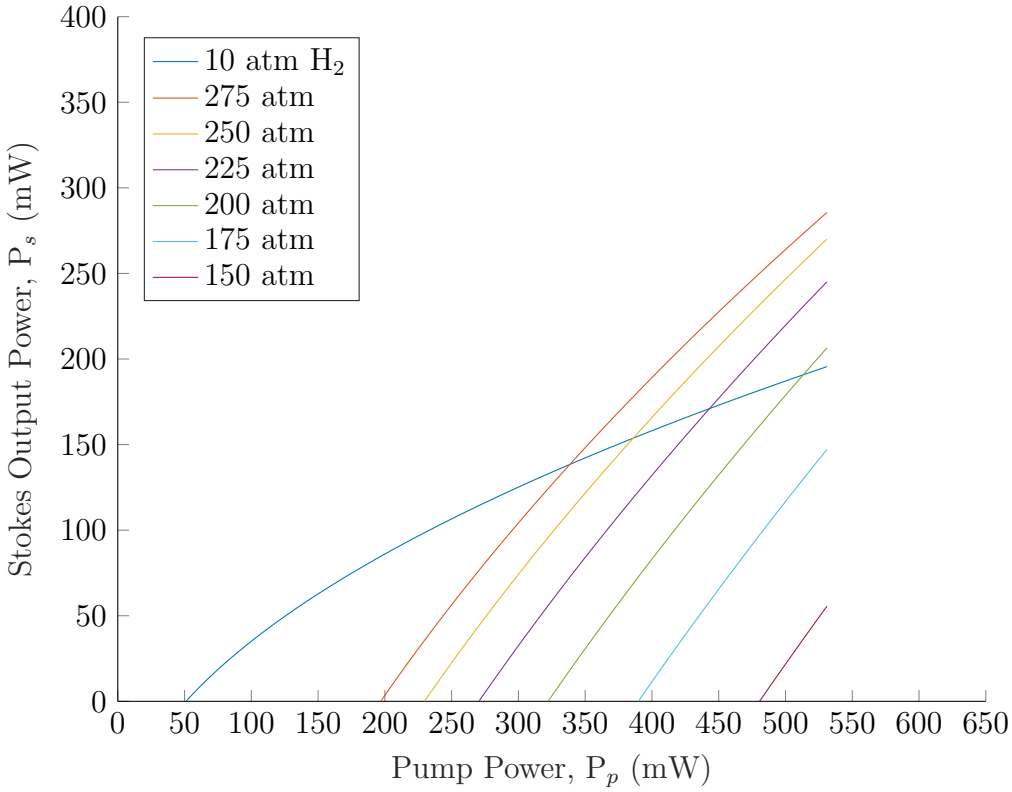

Figure 16. Using a 10 cm cavity length and pressures listed in the legend for nitrogen gas except the 10 atm line which is hydrogen gas. The output produced from the Verdi pump is expected as shown. The increasing pressure improves maximum output power of the nitrogen Stokes line with 250 atm producing more power than the hydrogen Stokes line; though, the nitrogen line is expected at 607nm and the hydrogen is expected at 683 nm. The maximum input takes into account losses from the laser path prior to the cavity including the uncoated sapphire window and two steering mirrors, and likewise the output takes into account the window and one steering mirror.

on the cross-section. Given this, the cross-section was taken as $\sigma(\lambda) = \sigma_0 \left(\frac{\lambda_0}{\lambda}\right)^4 m^2$, where σ_0 was 5.61×10^{-31} and λ_0 was 514.5×10^{-9}. Because Rayleigh scattering is angularly dependent as $1 + cos^2(\theta)$, where θ is in relation to the direction of propagation, the maximum angle able to stay in the cavity needed to be determined, in this case 0.07 radians. This meant that about 95% of the scattering was lost. Given this update to the model, it is unsurprising that the experiment did produce lasing at the pressures and pump power available. The current setup can exceed the threshold of 17.5 W from the Verdi pump in a 10 cm cavity with a pressure of 3800 psi, which is

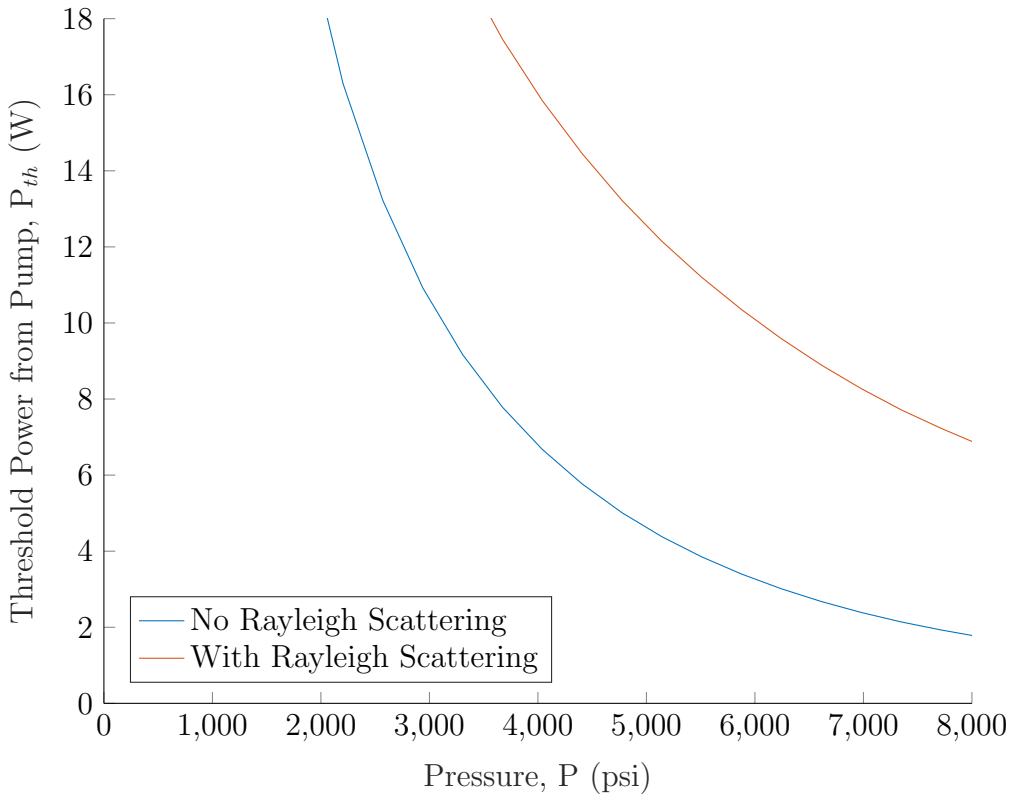

Figure 17. Shows the threshold power needed to pump into cavity given the pump losses prior to entering the cavity as a function of N_2 chamber pressure. The 10 cm cavity has lower mirror losses due to longer times between hitting the mirrors but has decreased intensity due to the less focused beam. This shows up in the model with and without the Rayleigh scattering being farther apart than the 4 cm cavity but no major change in the Rayleigh scattering included model between the two lengths.

close to the safety release point.

The previous articles did not need to include the Rayleigh scattering losses due to them using lower pressure at a maximum of 294 psi. The pressure dropping by an order of magnitude plus the Rayleigh cross-section of hydrogen being approximately a fifth that of nitrogen. These two things together would result in there being almost no difference in the output without including Rayleigh scattering, which is exemplified by how the model predicts 20 atm hydrogen in the 10 cm experimental setup used earlier. Fig. 18 shows that outcome, which only has a noticeable change at nearly 10 times the threshold. Because the Raman gain scales with the intensity of the pump

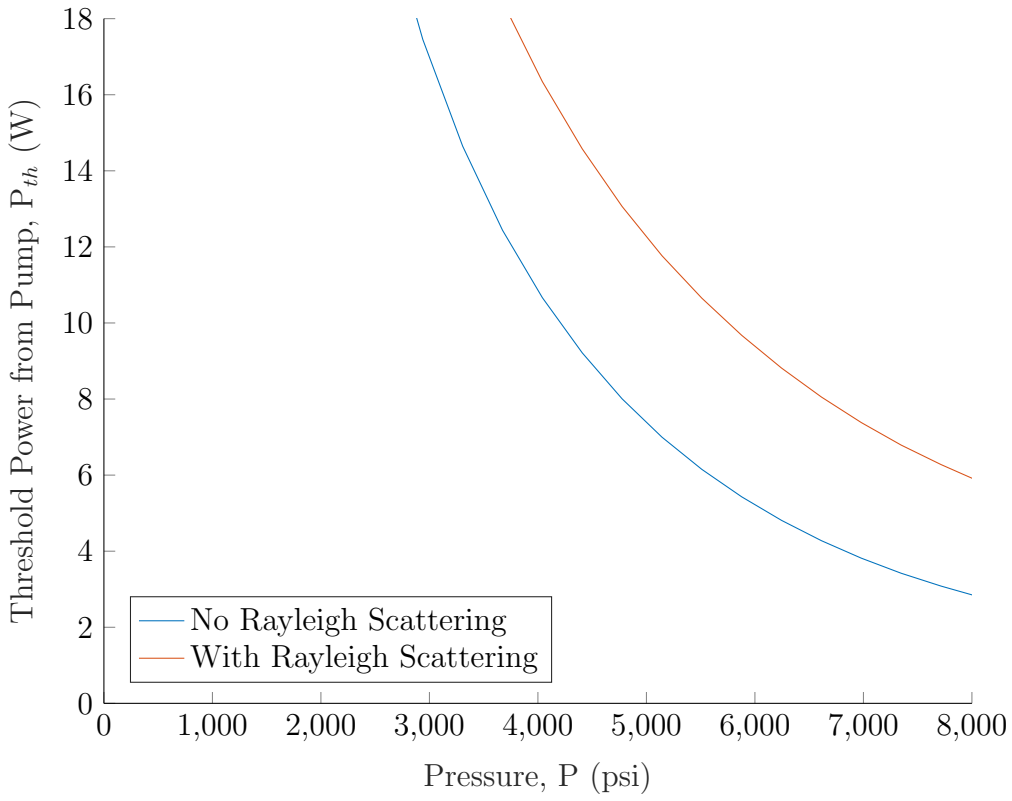

Figure 18. Shows the threshold power needed to pump into cavity given the pump losses prior to entering the cavity as a function of N_2 chamber pressure. The 4 cm cavity has a smaller minimum spot size for increased Raman gain but also has increased mirror losses due to shorter times between photons hitting the mirrors. This shows up in the model with and without the Rayleigh scattering being close together than the 10 cm cavity but no major improvement in the Rayleigh scattering included model between the two lengths.

as well as the stokes field, it is clearly that the key is maintaining minimal spot size for as long a gain length as possible.

5.2 Single-Pass Hollow-core Photonic Crystal

The initial model for the single-pass HCPCF takes eq. 3 and eq. 4 and divides each side by the speed of light to allow for a change of variable from dt to dz, which results in

$$\frac{dE_s}{dz} = (G \mid E_p \mid^2 E_s - L_s E_s) \left(\frac{1}{c}\right) \tag{19}$$

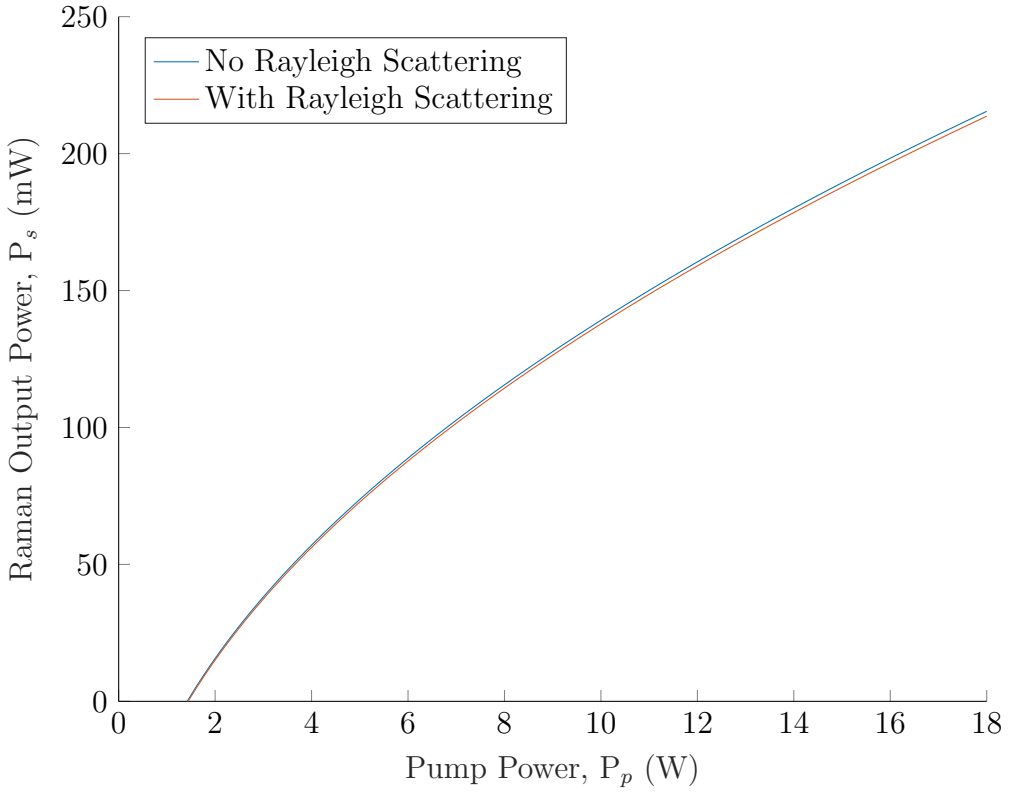

Figure 19. Model of 10 cm cavity at 20 atm in current setup with and without Rayleigh scattering. This shows how the hydrogen papers were easily able to ignore Rayleigh scattering as a loss mechanism in the cavity approach. The pump power is the power needed out of the 532 nm laser pump before any path losses or back reflection at the input coupler, and the output power is the power leaving the output coupler.

$$\frac{dE_p}{dz} = -\left(\frac{\nu_p}{\nu_s}\right) G \mid E_p \mid^2 E_s - L_p E_p) \left(\frac{1}{c}\right). \tag{20}$$

These are analogous to eq. 17 but in terms of field strength instead of intensity, and it ignores the rotational stimulated Raman which as previously noted is a good approximation with linearly polarized pump light and at high pressures. Both ignore another critical piece of information, the initial Stokes photons. One method would be to choose a seed field that matches experimental data and put it all at the front of the fiber. The other method would be to use the differential Raman cross-section along with the number denstiy and acceptance angle of the fiber. This will allow for approximating the field strength added to the stokes field along the path. The first

method would certainly be preferred if there were a seed laser being used, but the setup without a seed would have a better predictive output from the latter method. The spontaneous Raman field is

$$E_{sp} = \frac{\sqrt{\frac{1}{2}N\sqrt{\frac{\epsilon_0}{\mu_0}}E_p^2 \int (\frac{d\sigma}{d\Omega})d\Omega}}{\frac{1}{2}\sqrt{\frac{\epsilon_0}{\mu_0}}}, \tag{21}$$

where the field is converted to intensity then the whole thing is converted back. This can be greatly simplified by collecting terms and noting that the differential cross-section is not dependent on the solid angle to

$$E_{sp}(\Omega) = \sqrt{NE_p^2 \frac{d\sigma}{d\Omega}\Omega} / \sqrt{\frac{1}{2}\sqrt{\frac{\epsilon_0}{\mu_0}}}. \tag{22}$$

Now the field added to the stokes field must be taken from the pump field times the ratio of frequencies to conserve energy and all of the spontaneous Raman is lost not just the coupled filed, which results in

$$\frac{dE_s}{dz} = (G \mid E_p \mid^2 E_s - L_s E_s)\left(\frac{1}{c}\right) + E_{sp}(\Omega_{coupled}) \tag{23}$$

$$\frac{dE_p}{dz} = -(\frac{\nu_p}{\nu_s})G \mid E_p \mid^2 E_s - L_p E_p)\left(\frac{1}{c}\right) - \frac{\nu_p}{\nu_s}E_{sp}(4\pi). \tag{24}$$

These two equations govern the field through the fiber, but an additional number density dependent term was added to the loss like in the two-mirror cavity case, the Rayleigh scattering. Whereas the loss is typically thought of as being related to fiber material scattering and absorption and fiber confinement, HCPCF lasers need to be concerned with the gases scattering and absorption along with the fiber confinement. In the case of 532 nm pumped nitrogen, the absorption loss is negligible,

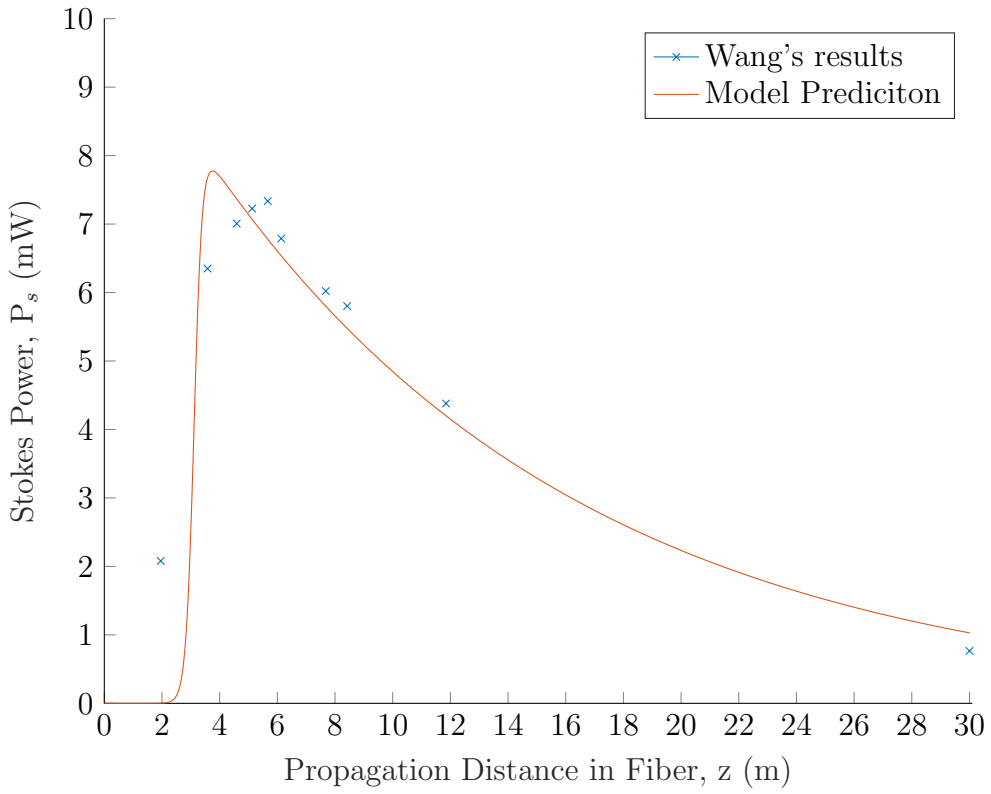

Figure 20. Model of 30 m H_2 HC-PCF with Wang et al's results put in for comparison. [4] The Model predicted a slightly earlier turn on but after the initial turn on the data matches closely.

but as previously shown the Rayleigh scattering loss can be quite high even with some recoupled into fiber in the forward direction. Explicitly, the losses are $L = L_{fiber} + L_{Rayleigh}$, where the fiber losses can be found in a vacuum or low pressure environment and the Rayleigh scattering losses will scale linearly with number density. If these equations are used on previous works, there is good agreement with Wang et all's results as seen in Fig. 20.

In the experiment attempted here, the updated model predicts that over 1 mW of SRS would be output from the 3 m of the Glophotonics fiber with a coupling efficiency of 40% at 2400 psi as seen Fig. 21. Given the same conditions except at 3500 psi, the SRS nears 1.4W from the fiber displayed in Fig. 22. Both of these graphs demonstrate clearly that the SRS in exponential growth in the short 3 m of fiber. A

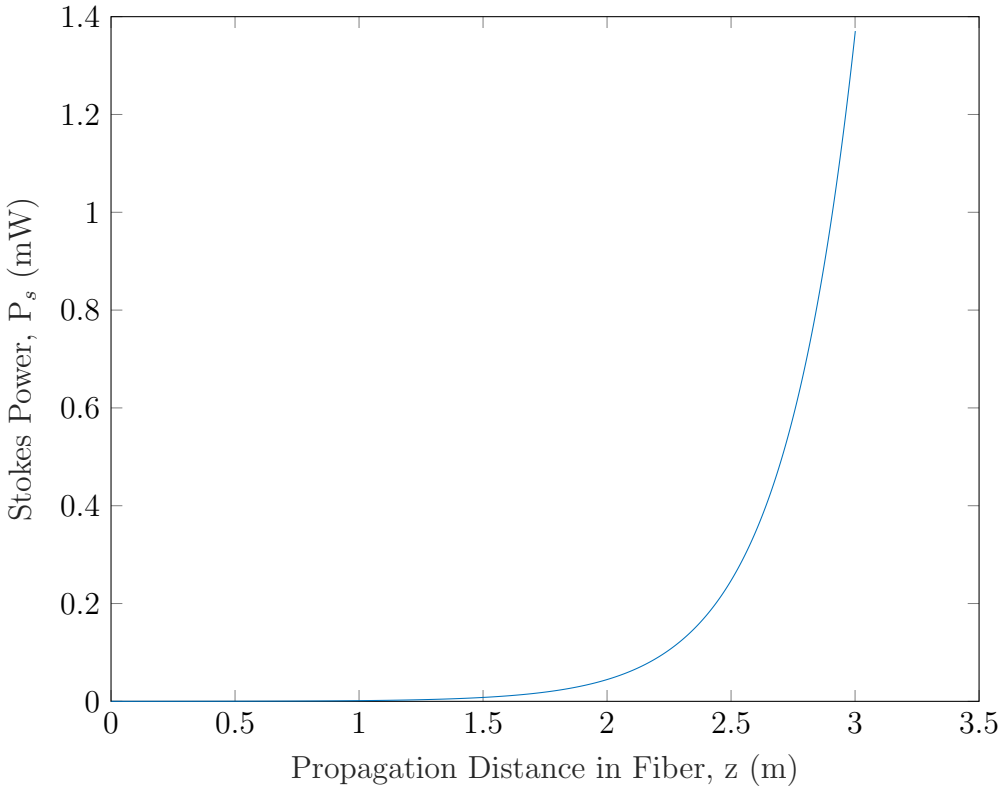

Figure 21. Model of the 3 m HC-PCF filled with 2400 psi of N_2. The lowest pressure that the output exceeds over 1 mW. The coupling efficiency was taken as 40% for this run to be conservative.

graph of pressure scaling shows an initial estimate of what it would take to saturate in the 3 m length. Fig. 23 shows that just over 4000 psi would be needed to convert the pump energy completely. Additionally, Fig. 23 shows how an O_2-filled HCPCF for comparison. O_2 always has less gain than N_2 as seen back in Fig. 3, but its lasing wavelength is shorter at 580 nm thus allowing for a higher conversion efficiency. The opposite side of the coin can be found using the model for H_2. The gain is higher, but the first vibrational line is at 683 nm. This together results in Fig. 24, where the Stokes beam maximizes conversion at less than 30 psi at a lower of overall power.

The other alternative to scaling the output power would be increasing the fiber length. At 1500 psi, the fiber would need to be approximately 15 m to convert the power to the Stokes wave, while the 3500 psi fiber prediction for saturation is close to

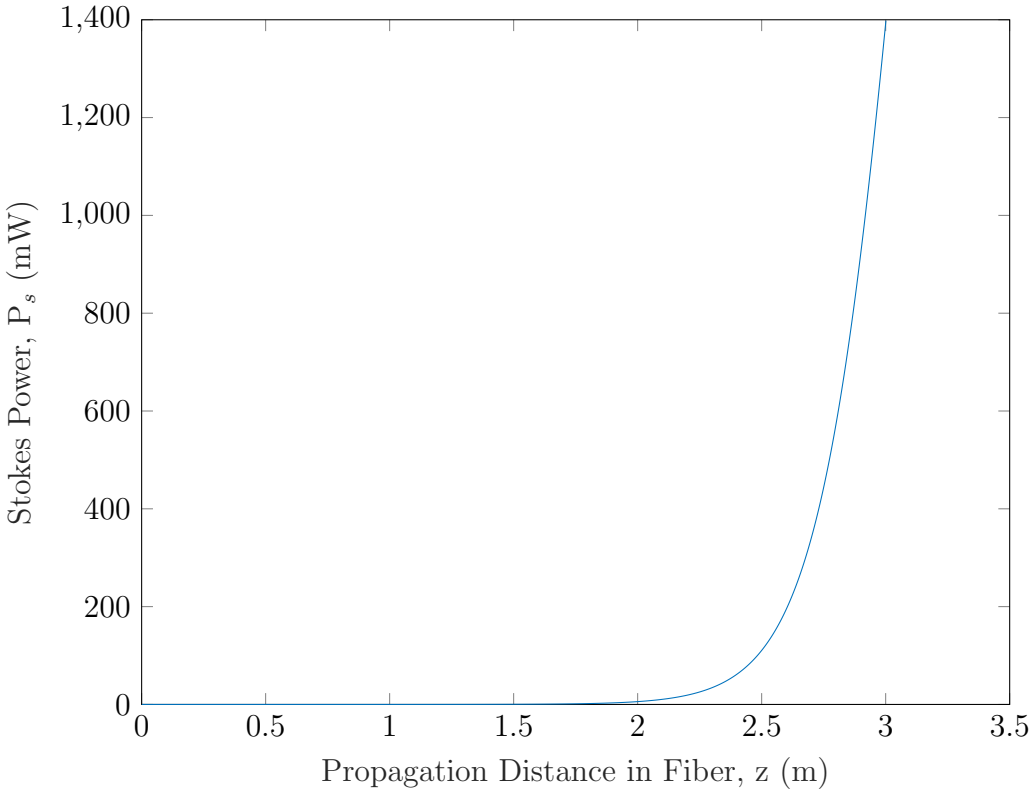

Figure 22. Model of 3 m N_2 HC-PCF at 3500 psi. The highest pressure reasonably attainable in the current chamber. The coupling efficiency was taken as 40% for this run to be conservative. By this pressure, it is approximately half way to the maximum value that it can ever achieve at around 3.7 W at the 607 nm given the coupled intensity.

5 m. O_2 always needs a longer fiber, but its gain scales at roughly the same rate as N_2, which keeps it close as seen in Fig. 25. Another way to view the trend of length and pressure would be to show the maximum power at those lengths, which better allows for the much lower pressure SRS from H_2 to be compared as in Fig. 26. This graph shows how N_2, O_2, and H_2 shrink to similar length needs at high pressures relative to the end of their respective line narrowing close to the quantum efficiency. The power increases due to the decrease in length over which losses are accumulating; though, losses per length are greater at high pressure due to the Rayleigh scattering.

Comparing N_2, O_2, and H_2 purely based on conversion misses a few of the benefits

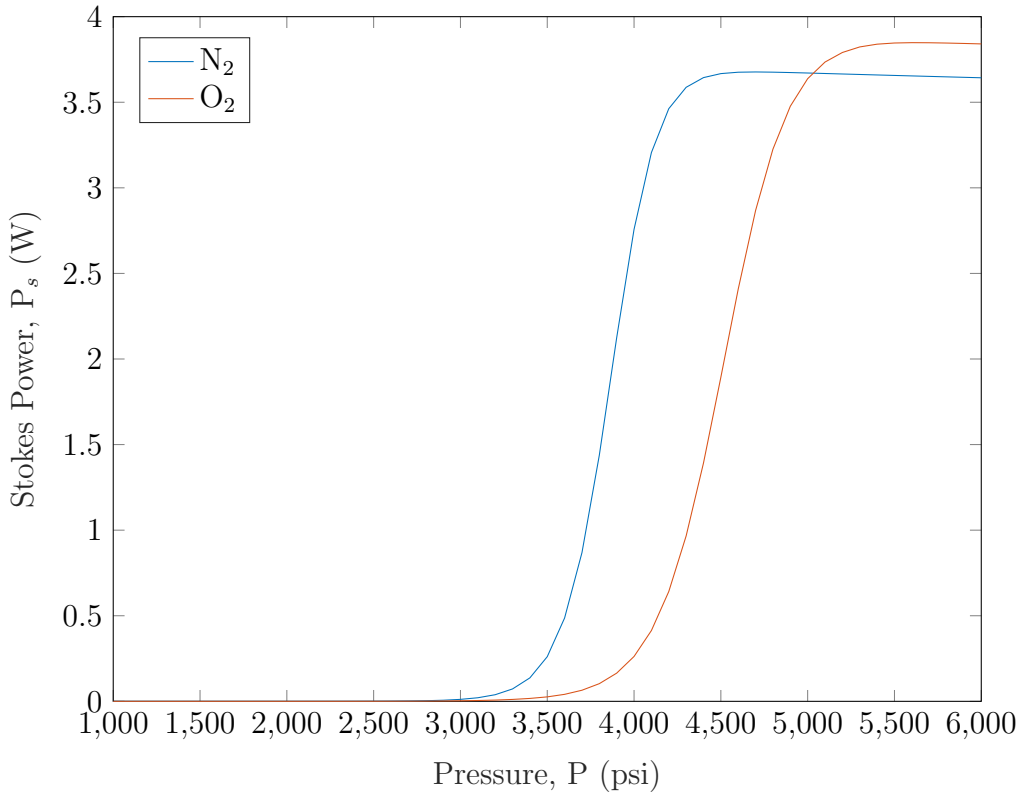

Figure 23. Model of 3 m N_2 HC-PCF up to 6000 psi. Shows how even the 3 m and 4000 psi of the experiment could demonstrate the potential of the system. The input was 16.5 W from the pump with 64% getting to the fiber and 40% coupling efficiency. O_2 requires higher pressure to get to saturation, but it can get higher due to its higher quantum efficiency stemming from its 580 nm stokes line instead of the 607 nm for N_2.

initially referenced for N_2. For instance, many materials become fuel for fire in very high O_2 enviroments including steel, so systems would require more expensive composites to house the O_2-filled HCPCF. H_2 is extremely reactive and requires equal levels of vigilance to prevent fires. Inert molecular nitrogen on the other hand is a high percentage of the atmosphere and creates no higher risk than of the containment bursting from the pressure.

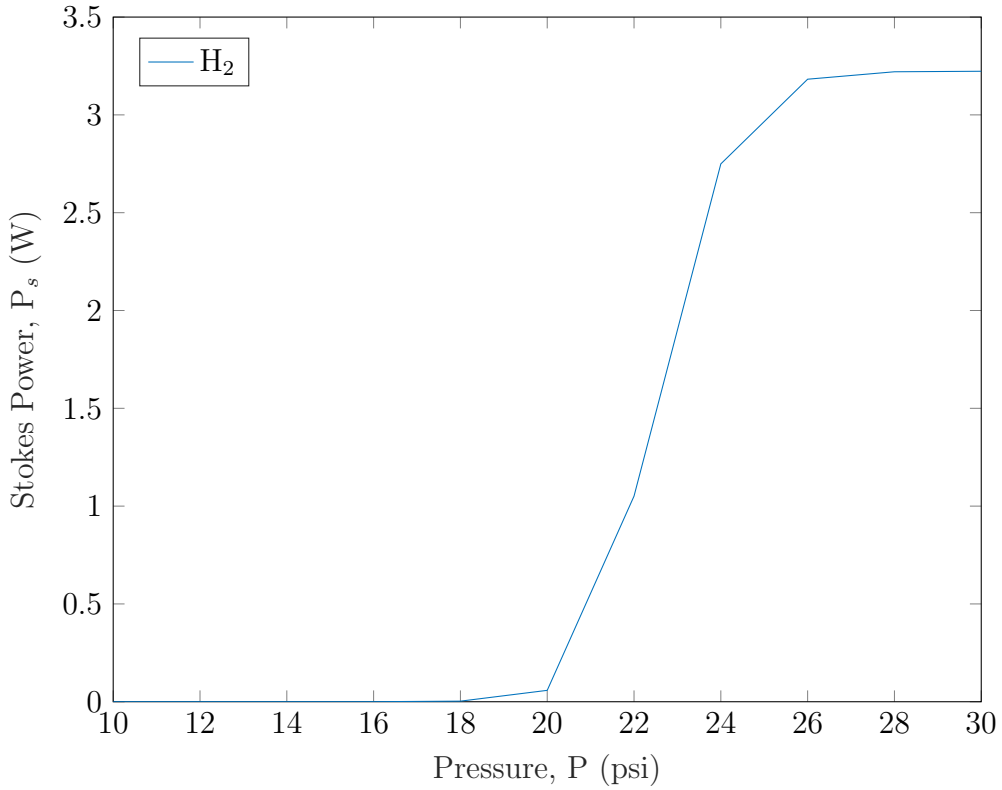

Figure 24. Model of 3 m H_2 HC-PCF up to 30 psi that shows how the additional gain leads to lower pressure maximization of conversion but how the large energy shift results in lower maximum powers.

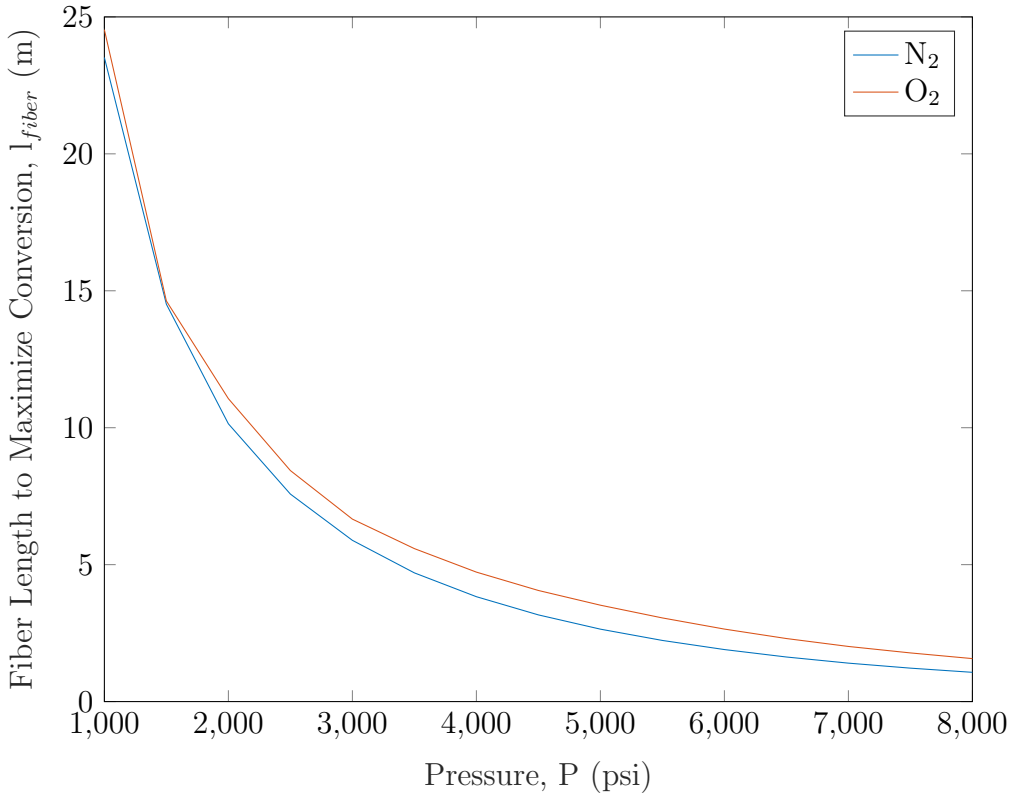

Figure 25. Single-Pass HC-PCF mode showing fiber length needed to maximize conversion with scaling pressure of N_2 and O_2.

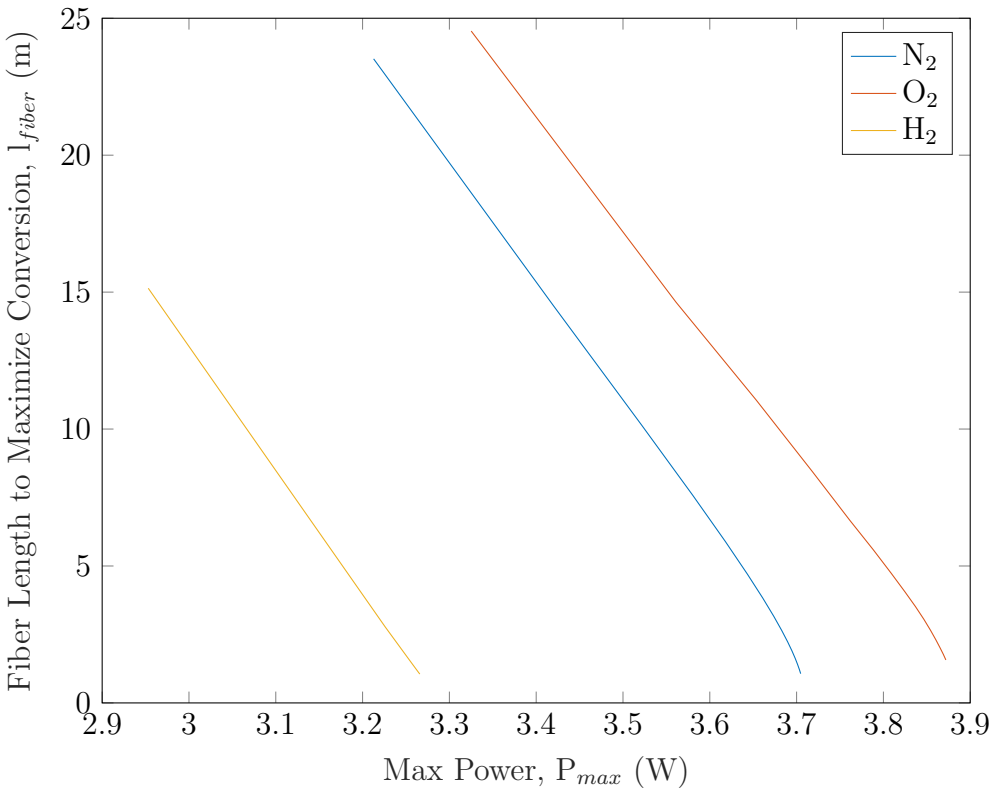

Figure 26. Model of N_2, O_2, and H_2 filling an HC-PCF up to where gain maximizes in a fiber long enough that they can always maximize conversion but no longer. It shows how much power could ever possibly come out of a fiber with this loss profile and pump. Each assumes the same input intensity as previously discussed and pumped at 532 nm with lasing to 607 nm, 580 nm, or 683 nm, respectively. Each improves output power as well as lowers the fiber length needed to get to that value with increased pressure.

VI. Conclusions

Gas chambers were built to test CW nitrogen SRS in a two-mirror cavity and single-pass HC-PCF. Neither produced lasing, but both led to improved understanding of what is needed to design a SRS laser system. From the cavity system, it became obvious from the bright scatter of the pump light that Rayleigh scattering would be a major loss source in nitrogen SRS at such high pressures that will need to be taken into account. This was confirmed with the single pass through the chamber scattering experiment which showed the rise in the Rayleigh scattering as a function of pressure. The increasing orange at 607 nm in both the cavity and the chamber scattering experiment show that more Raman scattering is also available at these higher pressures. The solution to tipping this further in favor of the SRS will be reducing the spot size as much as possible to increase the intensities of both the SRS and the pump. In a cavity, that means mirrors with higher radi of curvature and smaller cavities which will limit the total gain volume. To increase the gain volume, HC-PCFs with their long gain lengths could be the path forward for SRS lasers. HCPCFs have their own issues such as sensitive coupling to a fiber end and are not stable enough with high gas flow from leaking or filling. The motion of the fiber end can be mitigated with a smaller chamber and better mounting for the fiber ends. Smaller chambers also should allow for a more easily sealed window interface. A permanently sealed chamber on each side might seem enticing, but the ability to take out the fiber and hold it in place is still of critical importance in case of damage to fiber ends where recleaving is necessary. Future work should make design decisions based on the knowledge that leaks can be crippling to coupling into the fiber; thus, a top priority for any chamber is the ability to completely seal the chamber. The ability to hold much higher pressures securely would be a huge boon for nitrogen SRS lasing. At the pressures tested, the gain was less than the hydrogen at the 294 psi where it flattens out, which means

the benefits from using nitrogen were just the slightly smaller wavelength shift and the inert gas safety.

The updated model more closely aligns with experiments, hopefully improving future designs for a nitrogen vibrational SRS laser. In the cavity case, the update of Rayleigh scattering allows for better understanding of the trade space of round trip losses with respect to the cavity length versus resonant spot size. This would allow for better selections in mirrors, particularly their curvatures. The updates to the HCPCF model allow for more concrete initial conditions for the unseeded case based on the numerical aperture of the fiber, the differential Raman cross-section, and the number density inside the fiber. It also added Rayleigh scatting losses based on the numerical aperture, which can be significant for the number densities necessary for N_2 SRS compared to only including fiber confinement losses. Based on the model, it is clear that a HC-PCF would be an appropriate method for getting to CW nitrogen SRS lasing. A longer fiber would get to nearly complete conversion of the pump laser even at lower pressures as low as 1500 psi.

Future work should focus on the HC-PCF approach. More specifically, fiber lengths should be chosen based on the the desired number density and pump wavelength to allow for maximum conversion. Demonstration of CW N_2 SRS operation at any wavelength would be a major step, but particularly with stronger pumps in the infrared. This could prove the value of nitrogen SRS lasing by achieving highest single device powers at numerous wavelengths based on high-conversion efficiency from available pump wavelengths to non-available wavelengths. This would demonstrate its broad wavelength agility for various applications. Another path would be investigating extremely high pump powers in the near infrared for maximum single channel power. HC-PCFs can have lower losses than traditional single-mode optical amplifiers, but little research has been done on how they would actually perform

under such conditions. A more theoretical avenue for future research would be an increased understanding of achieving the mode output from HC-PCFs. During this work, multi-mode operation was always observed despite the manufacturers specifications on the output field appearing to be Gaussian. Any power scaling would need to understand what coupling parameters matter most for getting a single Gaussian mode out.

Appendix A. Scattering Images

This appendix includes a selection of images from the time evolution of the scattering experiment. Each has a title on the image with the pressure of the cell when the image was captured. The purpose is to get a visual feel for the increase in the scattering with pressure as opposed to numerical evaluation given in the results section of this work. The first 6 are back scatter images with a 550 nm high pass filter with the first being a raw image. The next 5 are the accompanying forward scatter images with the first being a raw image. Followed by 6 Rayleigh scattering images with 550 nm low pass filter with the first being a raw image. The next 6 are the forward scattering images to match with the first being a raw image.

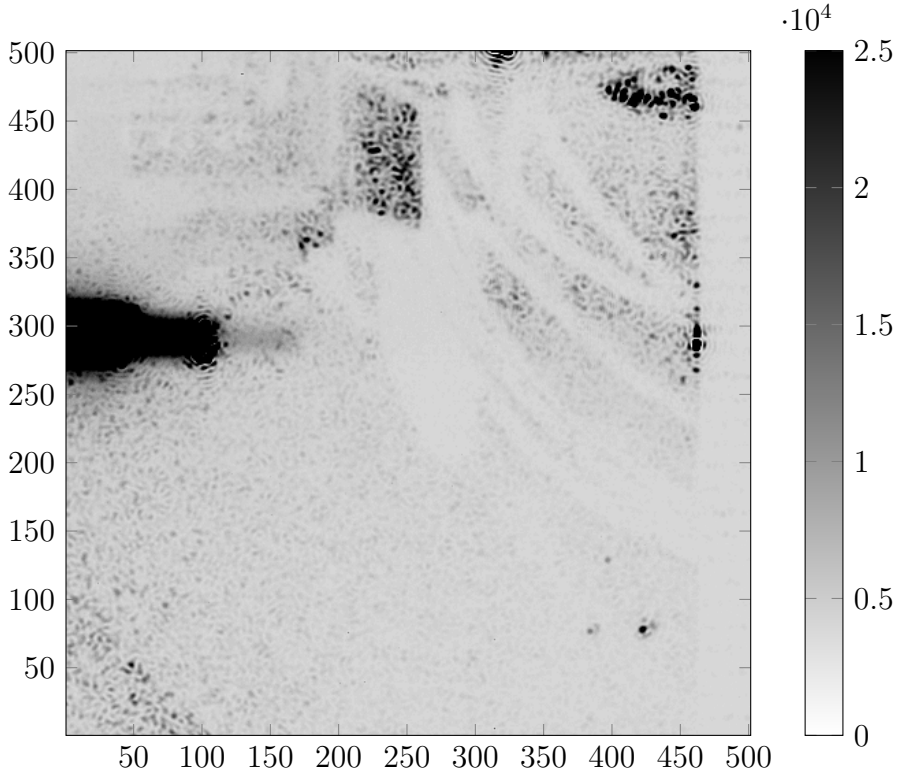

Figure 27. The Raman back scatter unfiltered image hows the portion of interest without any digital filter at a rough vacuum. The bright spot is the red scattering from the titanium in the window. The small tick mark on the far right of the screen are from a ruler for scale and to block high reflections from stray light off the cavity mirror, which is in the chamber. The wires provide the input to the electrically controlled mirror mounts.

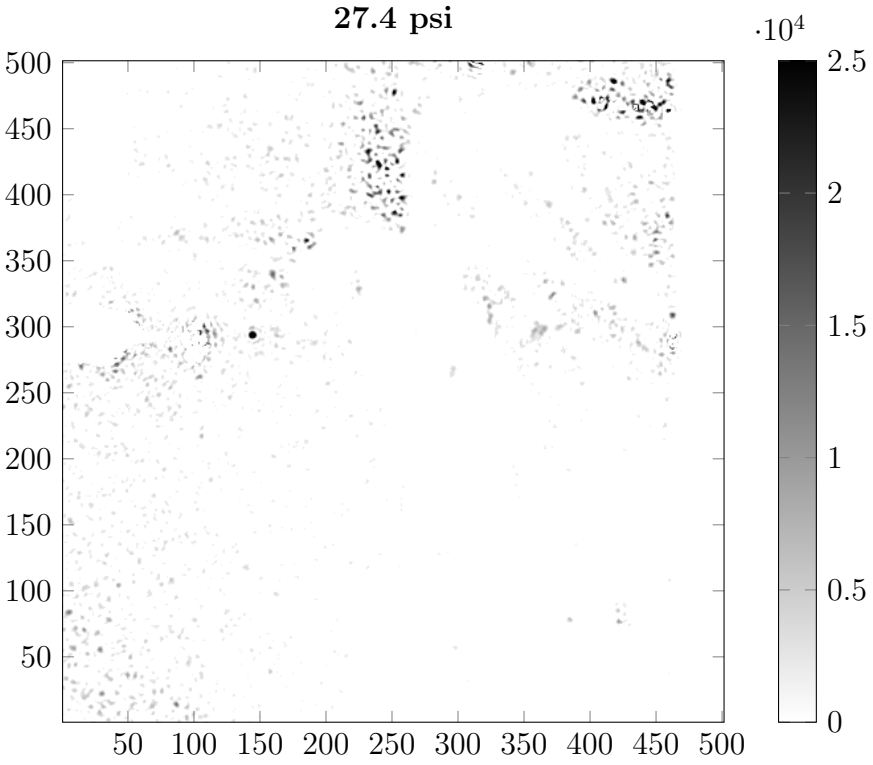

Figure 28. The Raman back scatter at 27 psi shows effect of the background subtraction on the early frames. At 27 psi, the image is basically just noise, and the red from the impurity is not seen.

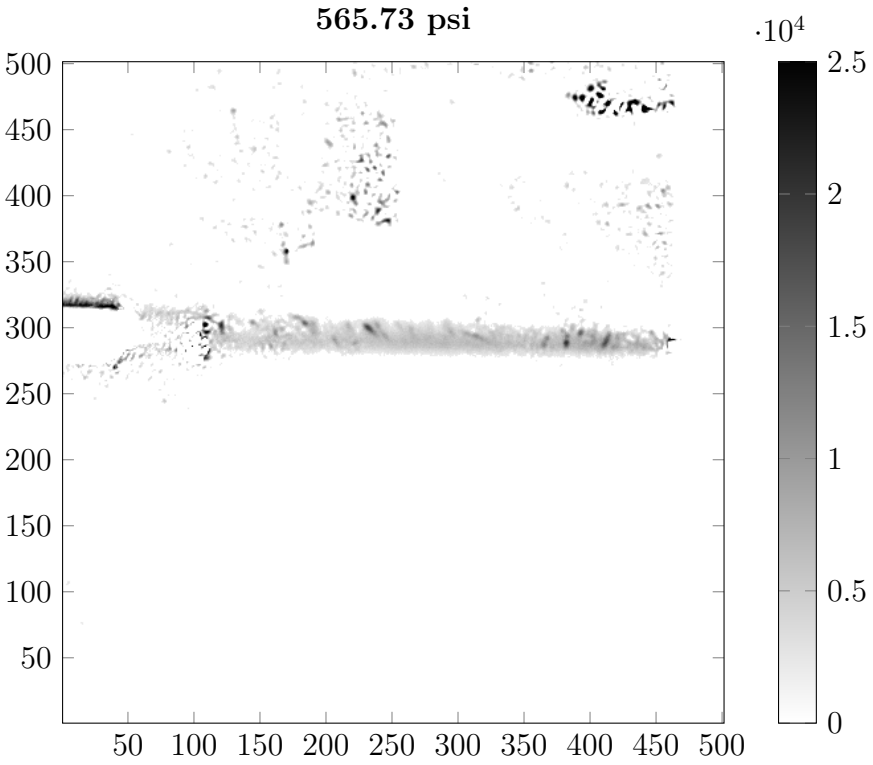

Figure 29. Raman back scatter at 565 psi shows the beam starting to appear on the color map that is held constant for all of the Raman back scatter plots.

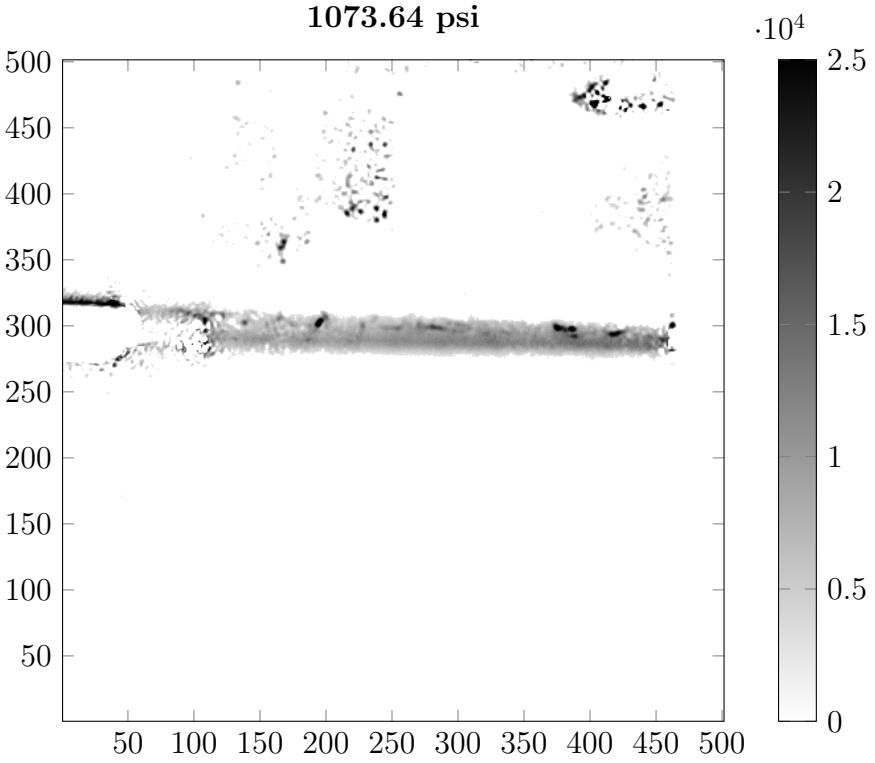

Figure 30. Raman back scatter at 1073 psi shows the back reflection due to the high pressure. The bright portion on the right is the beam in the window with the impurity scattering that is just too high on the image to have been eliminated in the background subtract.

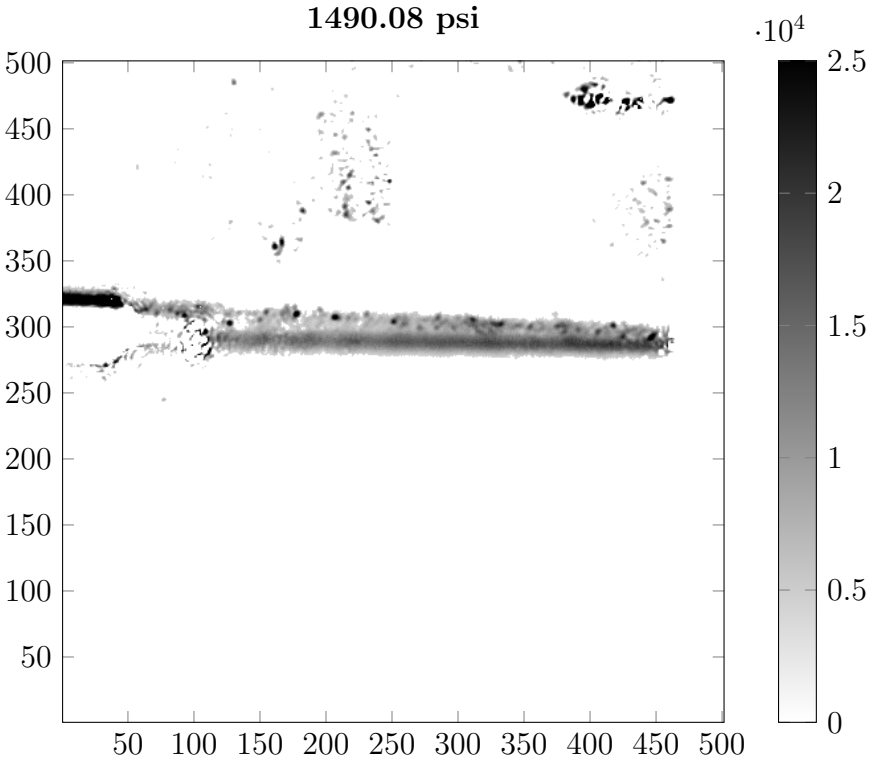

Figure 31. Raman back scatter at 1490 psi shows the back reflection due to the high pressure. The bright portion on the right is the beam in the window with the impurity scattering that is just to0 high on the image to have been eliminated in the background subtract. This is similar to the 1073 psi image but at a different point in the beam drift that was visibly evident with the flow rate.

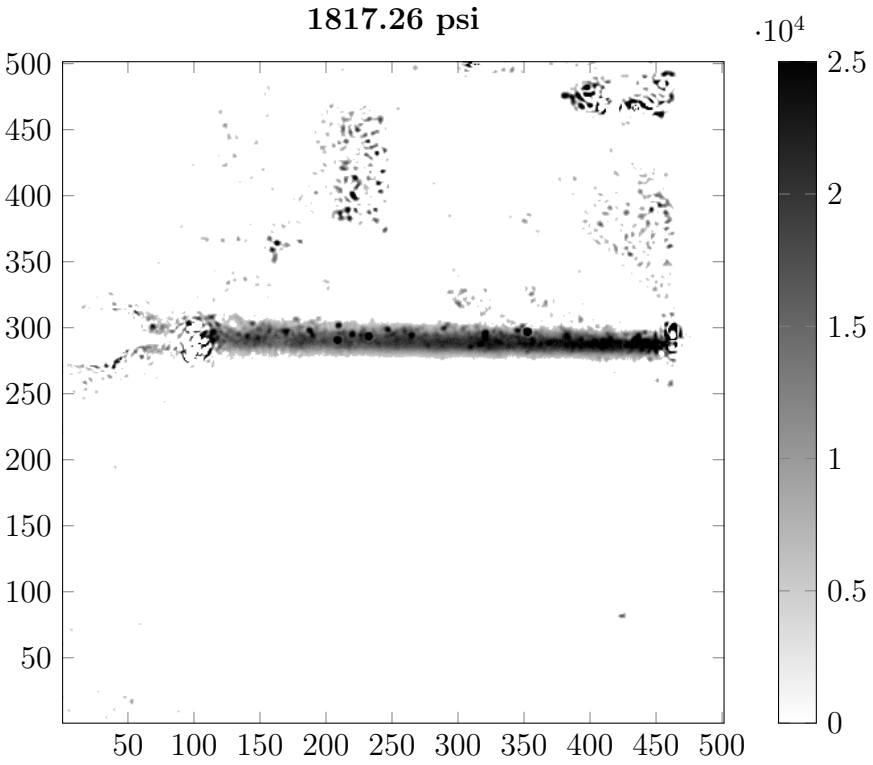

Figure 32. The Raman back scatter at 1817 psi ise the highest pressure Raman data collected due to large leak in one of the window's NPT connection to the chamber.

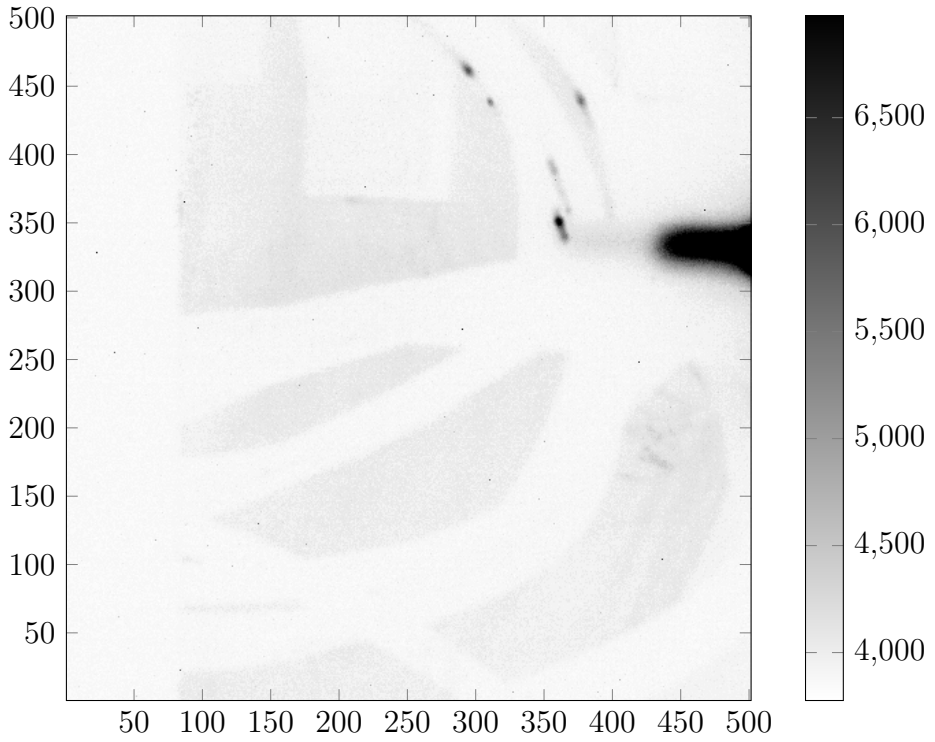

Figure 33. The Raman forward scatter unfiltered image shows the portion of interest without any digital filter at a rough vacuum. The bright spot is the red scattering from the titanium in the window. On the far left of the image is a ruler for scale and to block high reflections from stray light off the cavity mirror, which is in the chamber. The ruler's tick marks could not be made out due to the low brightness. The wires provide the input to the electrically controlled mirror mounts.

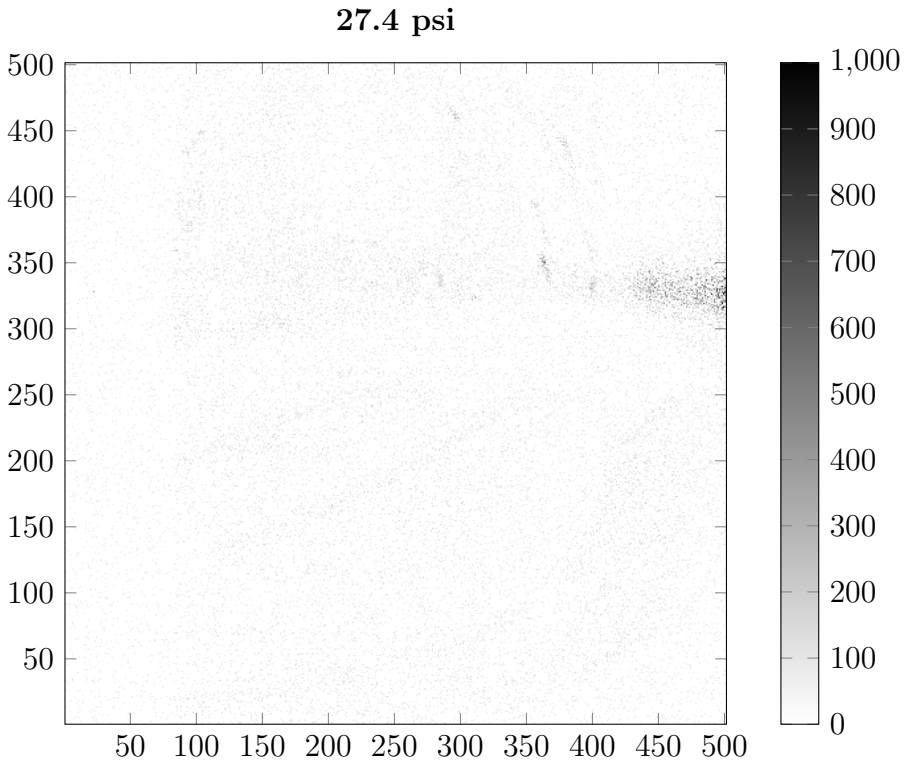

Figure 34. The Raman forward scatter at 27 psi shows effect of the background subtraction on the early frames. At 27 psi, the image is basically just noise, and the red from the impurity is not seen.

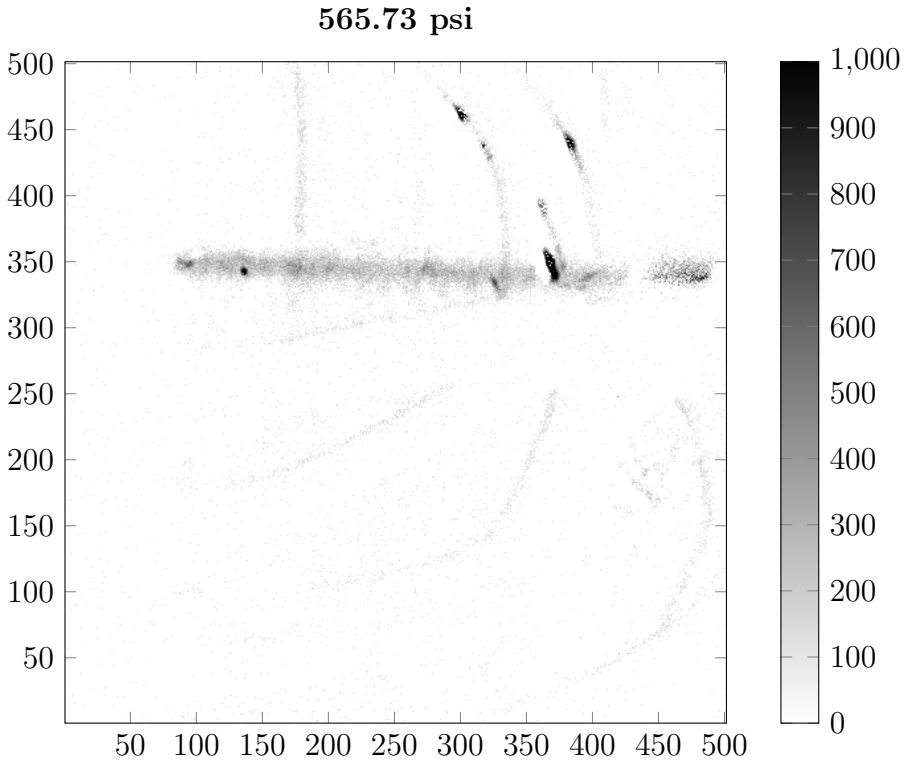

Figure 35. The Raman forward scatter at 565 psi shows the beam starting to appear on the color map that is held constant for all of the Raman back scatter plots.

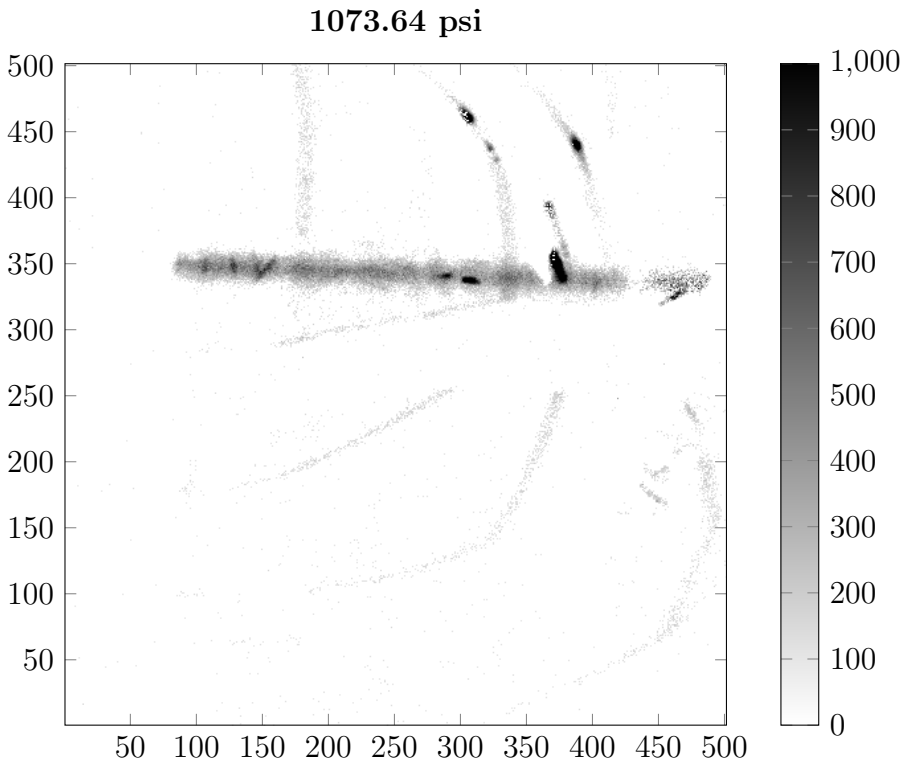

Figure 36. The Raman forward scatter at 1073 psi shows the beam begins to fill out the image more uniformly.

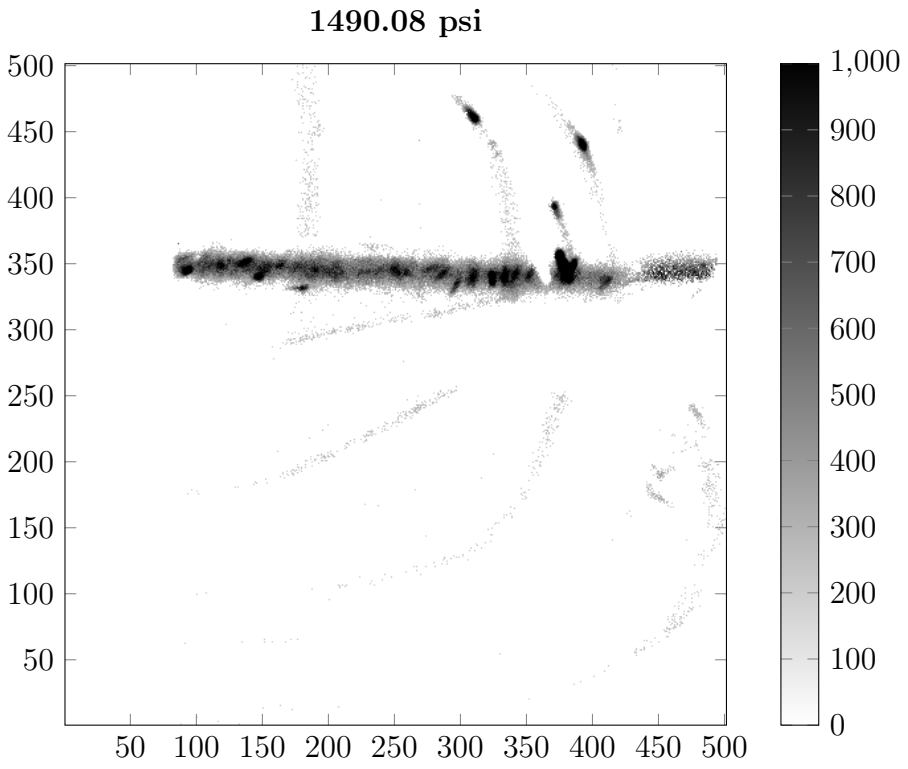

Figure 37. Raman forward scatter at 1490 psi shows the distinct intensity profile of the beam with the center brightest and fading out.

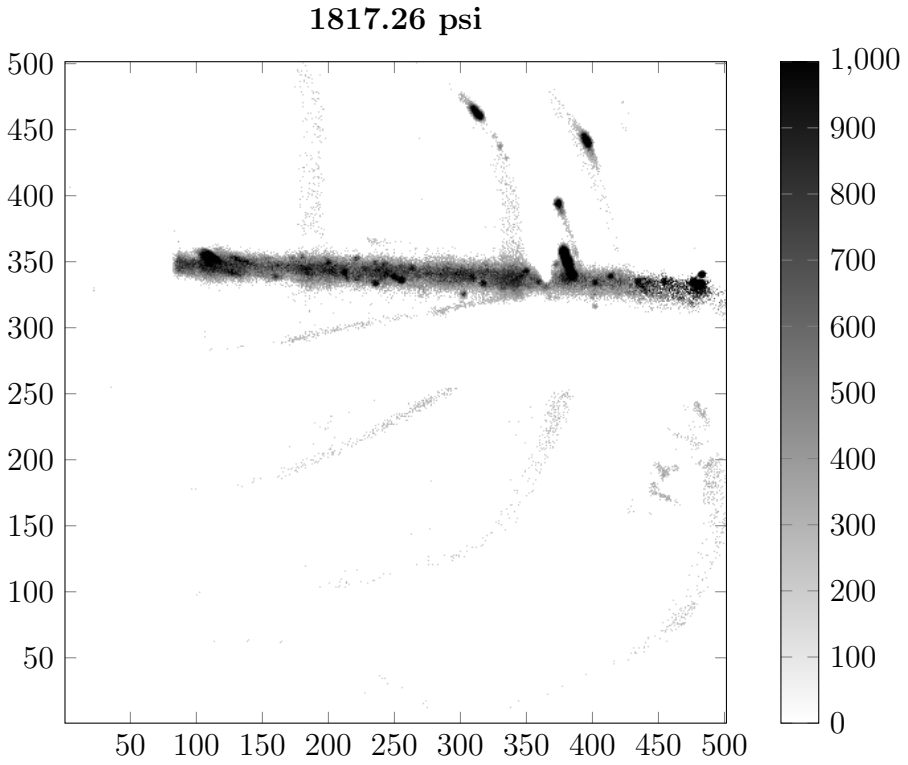

Figure 38. The Raman forward scatter at 1817 psi was the highest pressure data collected due to large leak in one of the window's NPT connection to the chamber.

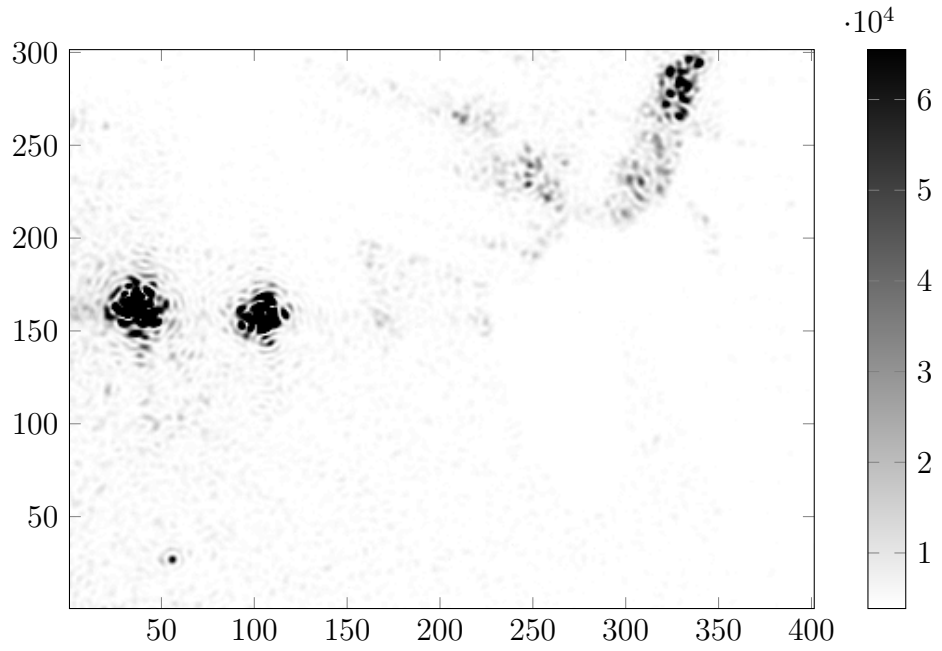

Figure 39. The Rayleigh back scatter unfiltered image shows the portion of interest without any digital filter at a rough vacuum. The image is very dark due to the ND 1 filter, the low Rayleigh scattering below atmospheric pressure, and the low pass filter blocking the titanium scattering in the window. The two bright spots on the left are reflections off the chamber's window on each side.

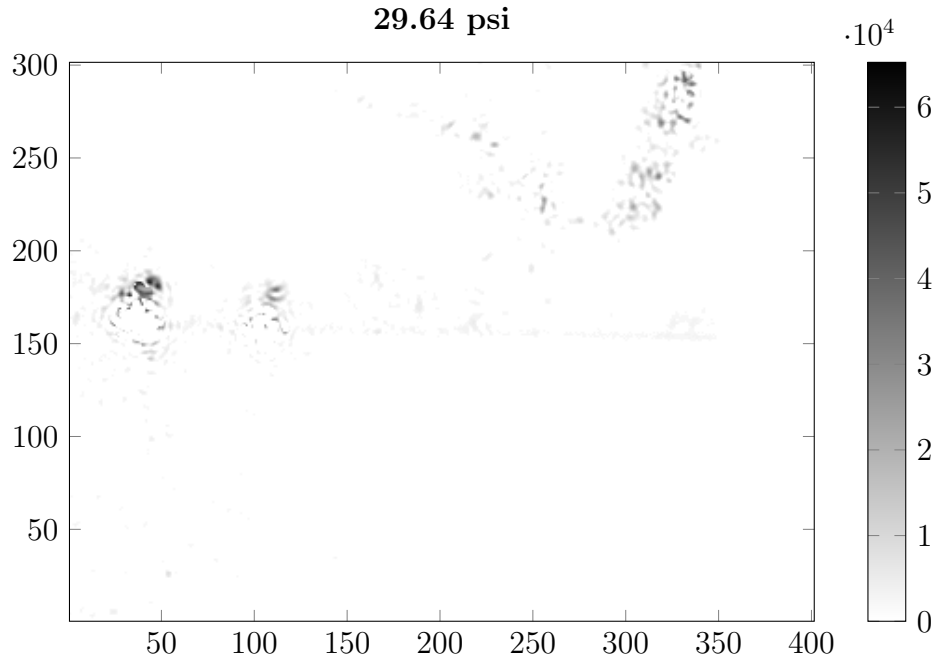

Figure 40. The Rayleigh back scatter at 29 psi displays image before beam shows up after the background subtract.

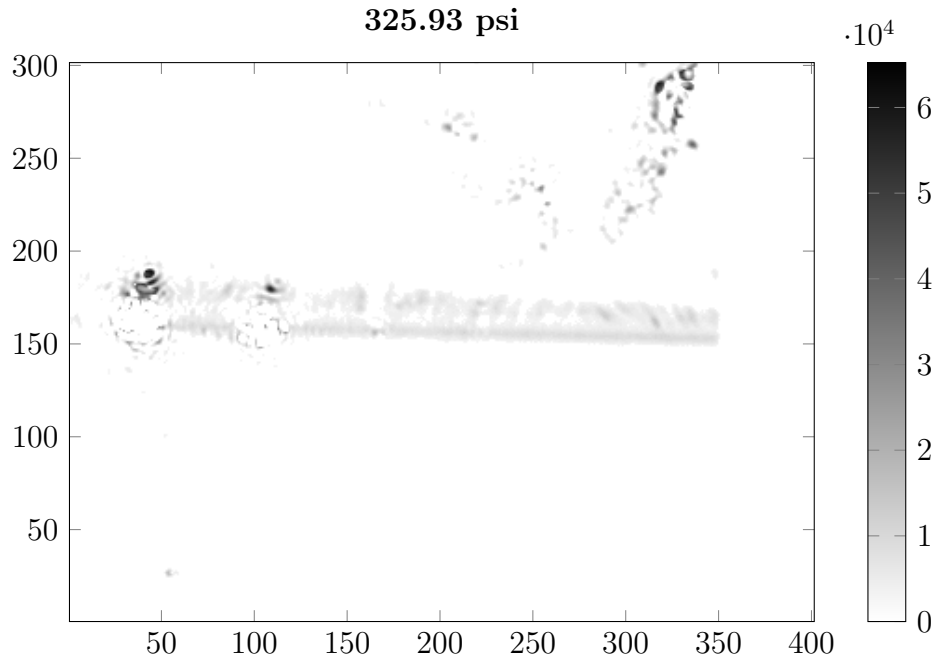

Figure 41. The Rayleigh back scatter at 325 psi shows the beam starting to appear along with the fainter back reflection off the back window.

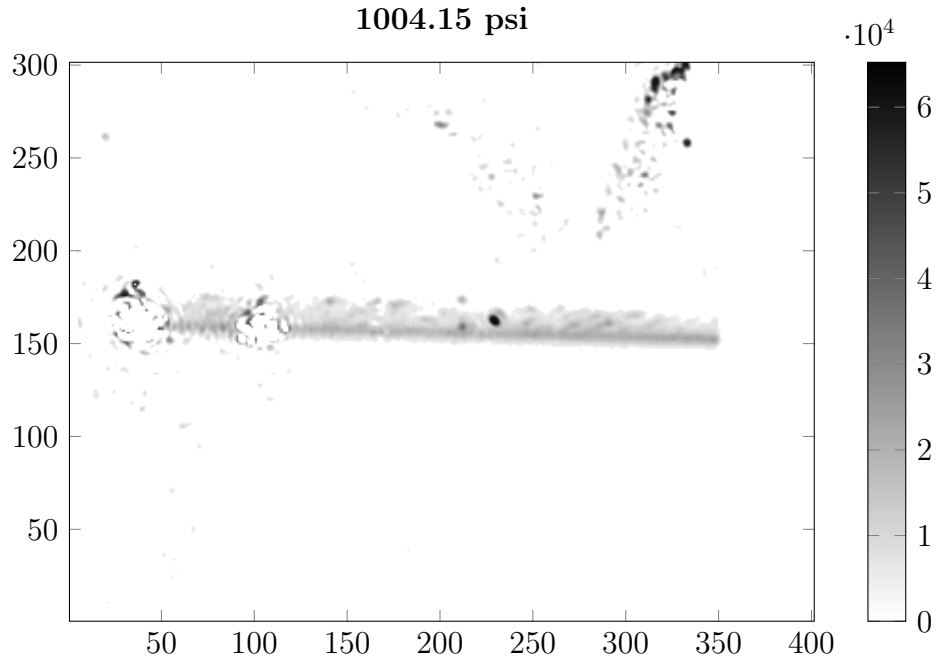

Figure 42. The Rayleigh back scatter at 1004 psi shows the scattering fill out.

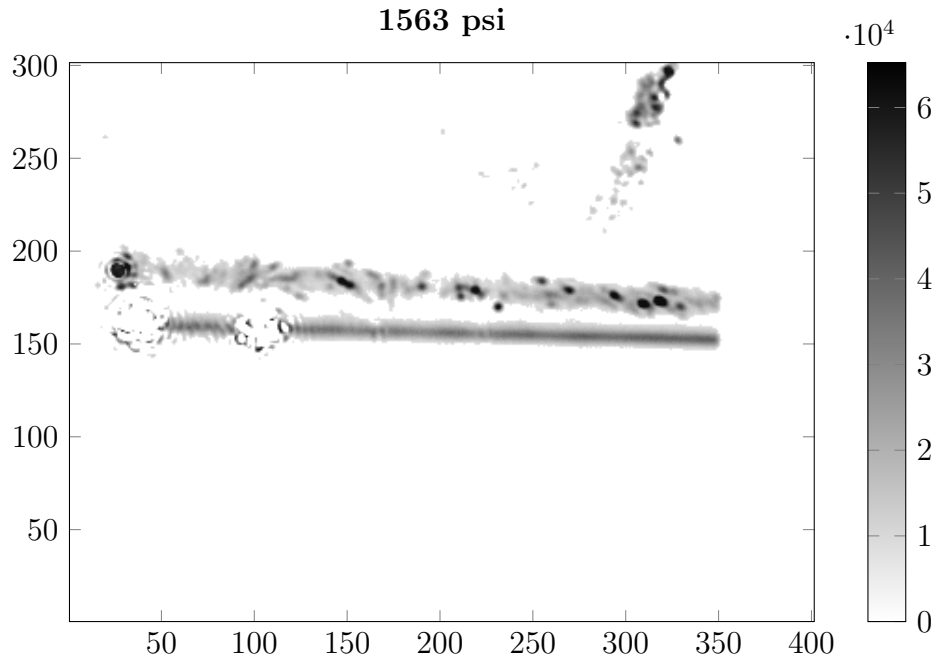

Figure 43. The Rayleigh back scatter at 1563 psi shows the back reflection's Rayleigh scattering strengthen.

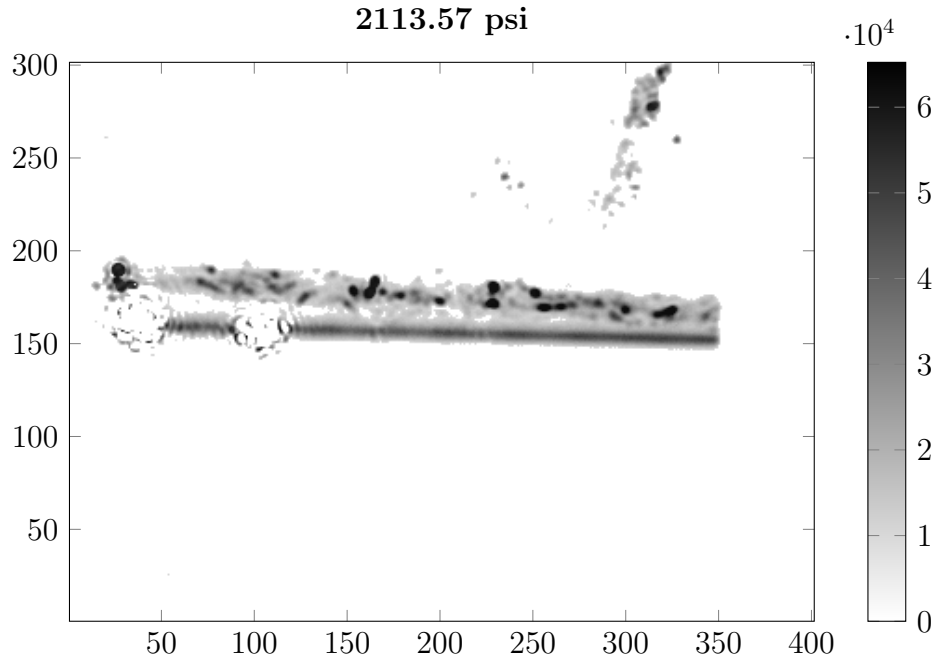

Figure 44. The Rayleigh back scatter at 2113 psi shows the back reflection's scattering continue to grow.

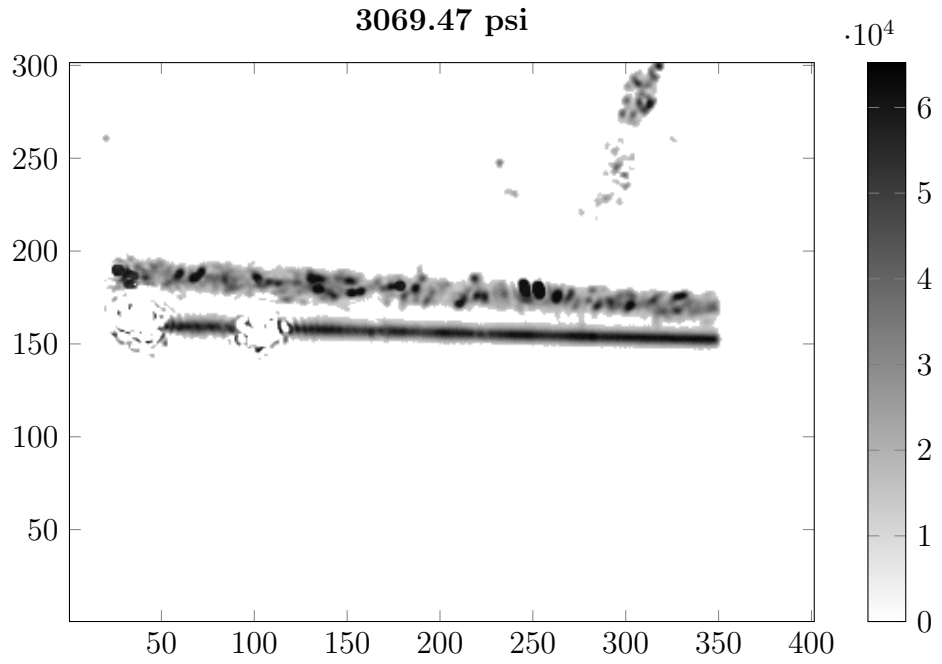

Figure 45. The Rayleigh back scatter at 3069 psi shows the back refelection increased at the highest pressure that collected.

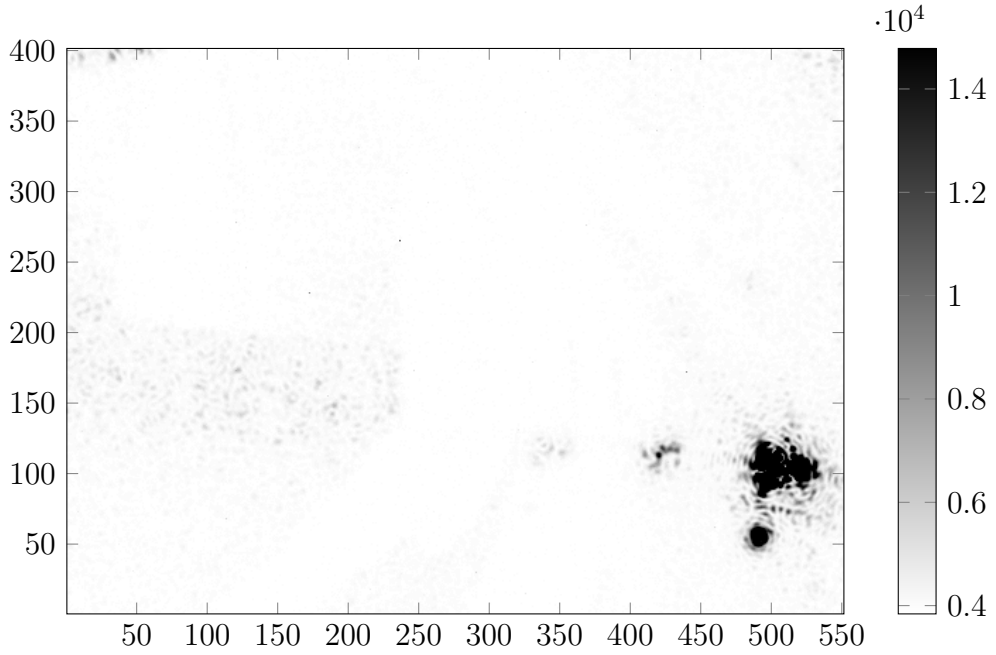

Figure 46. The Rayleigh back scatter unfiltered image shows the portion of interest without any digital filter at a rough vacuum. The image is very dark due to the ND 1 filter, the low Rayleigh scattering below atmospheric pressure, and the low pass filter blocking the titanium scattering in the window. The two bright spots on the right are reflections off the chamber's window on each side.

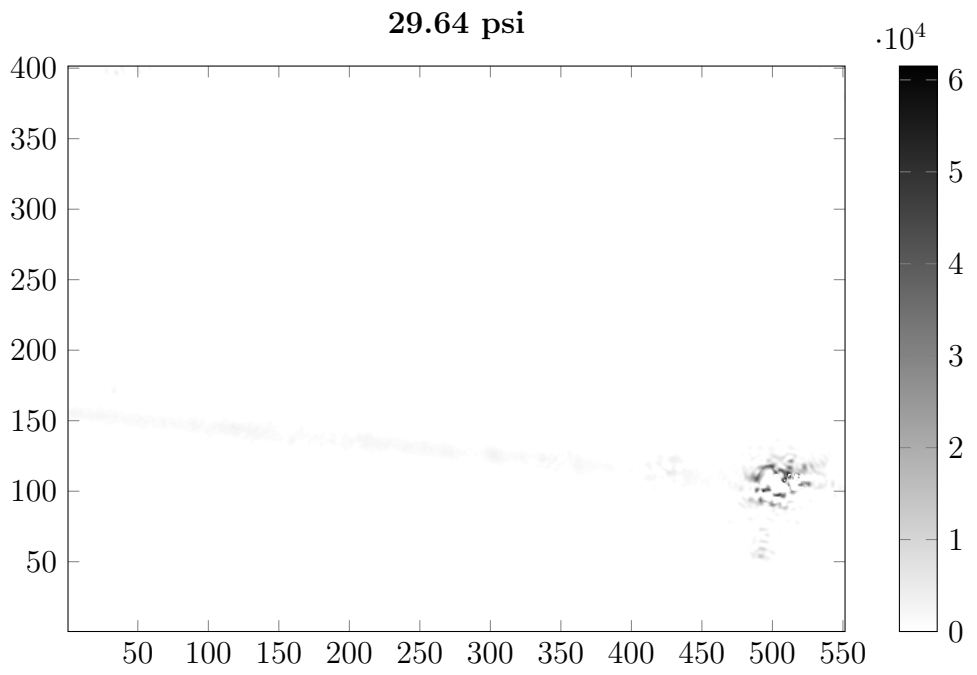

Figure 47. Rayleigh forward scatter at 29 psi displays image before beam at the beginning.

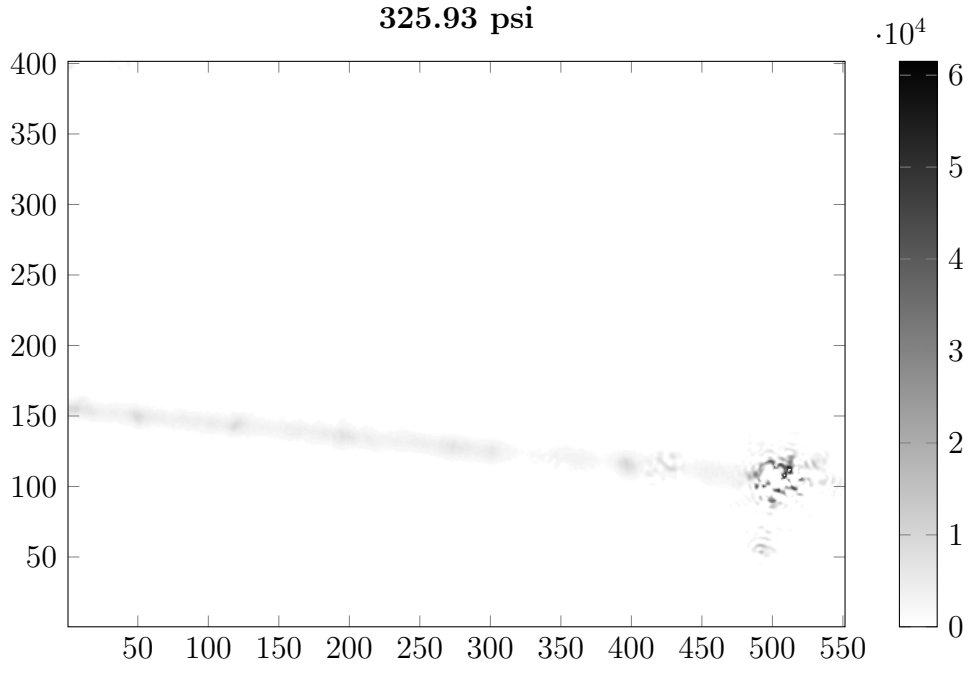

Figure 48. The Rayleigh forward scatter at 325 psi shows the beam start to appear along with the fainter back reflection off the back window.

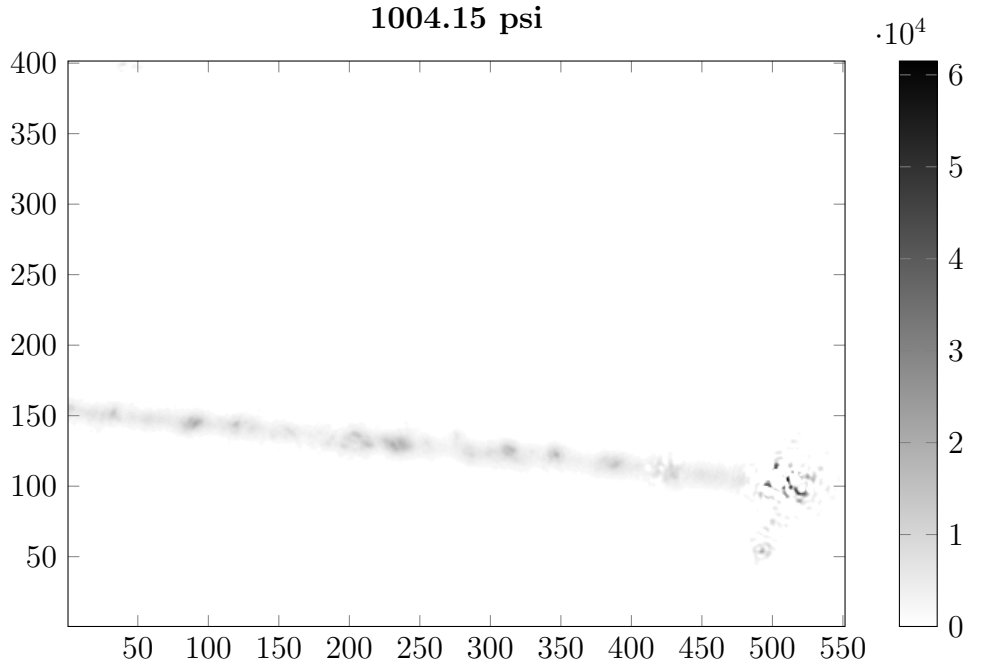

Figure 49. The Rayleigh forward scatter at 1004 psi shows that the scattering is still faint.

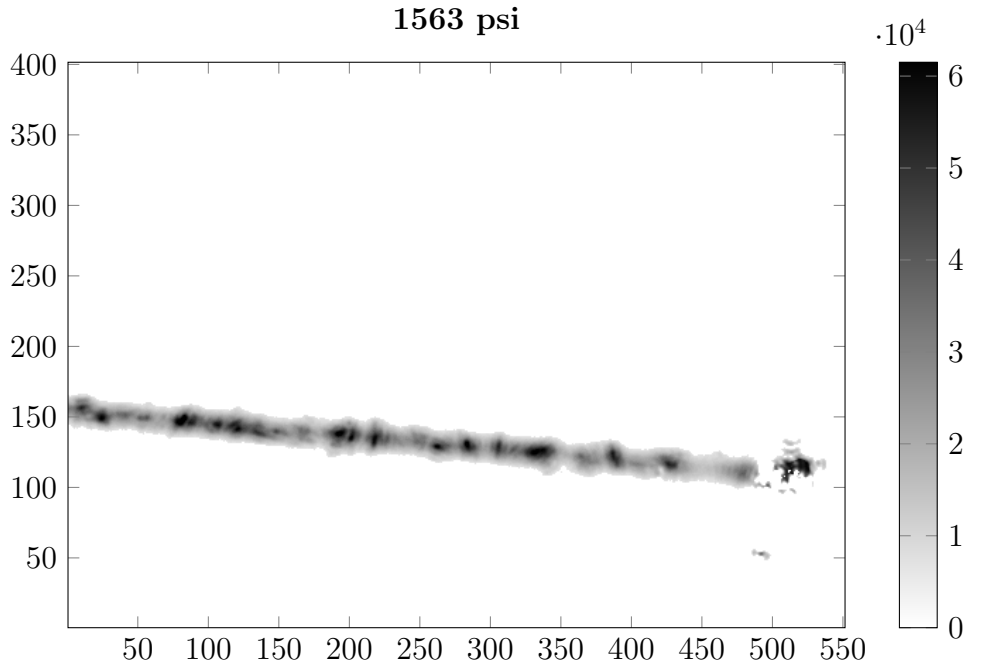

Figure 50. The Rayleigh forward scatter at 1563 psi shows the beam profile fill out.

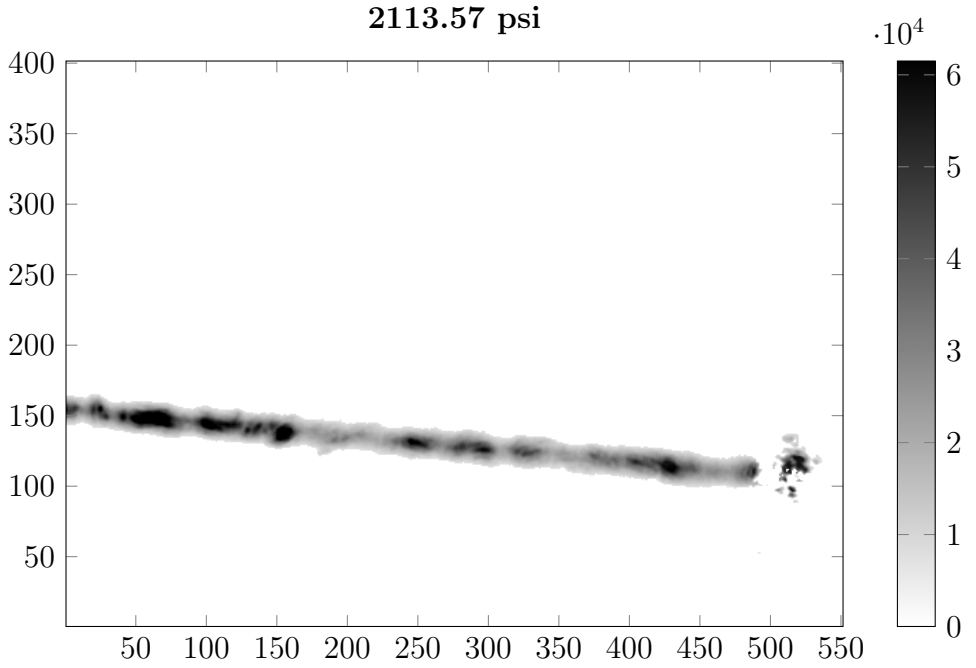

Figure 51. The Rayleigh forward scatter at 2113 psi shows the continued growth.

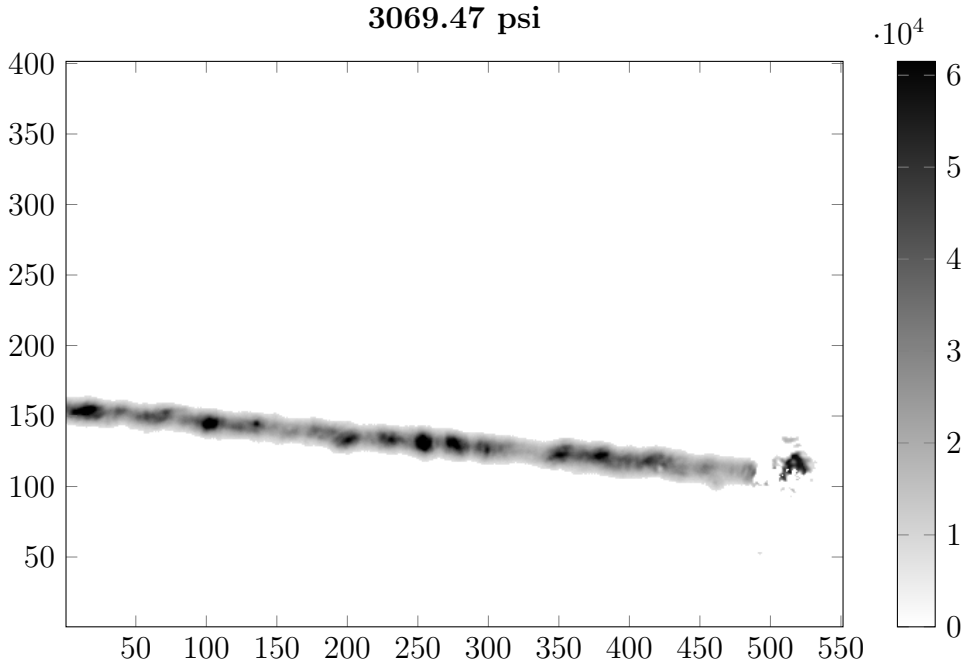

Figure 52. Rayleigh forward scatter at 3069 psi shows the Rayleigh scattering back continued at the high pressure that collected.

Bibliography

1. W. K. Bischel and M. J. Dyer, "Temperature dependence of the raman linewidth and line shift for the q(1) and q(0) transitions in normal and para-h_2," *Phys. Rev. A*, vol. 33, pp. 3113–3123, May 1986.

2. B. Lavorel, R. Saint-Loup, and H. Berger, "stimulated raman spectroscopy of the q-branch of nitrogen at high pressure," *molecular physics*, vol. 75, no. 2, pp. 397–413, 1992.

3. G. Millot, C. Roche, R. Saint-Loup, R. Chaux, H. Berger, and J. Santos, "Collisional narrowing and shifting in the Raman Q-branch of oxygen at high density," *Chemical Physics*, vol. 173, pp. 505–512, 1993.

4. Z. Wang, F. Yu, W. J. Wadsworth, and J. C. Knight, "Efficient 1.9 μ m emission in H ₂ -filled hollow core fiber by pure stimulated vibrational Raman scattering," *Laser Physics Letters*, vol. 11, no. 10, p. 105807, 2014.

5. G. P. Perram, M. A. Marciniak, and M. Goda, "High-energy laser weapons: technology overview," *Laser Technologies for Defense and Security*, vol. 5414, no. March 2016, pp. 1–25, 2004.

6. J. Judson. (2016) Dod presses on in pursuit of laser weapons. [Online]. Available: https://www.defensenews.com/smr/space-missile-defense/2016/08/24/dod-presses-on-in-pursuit-of-laser-weapons/

7. B. Debord, F. Amrani, L. Vincetti, F. Gérôme, and F. Benabid, "Hollow-Core Fiber Technology: The Rising of "Gas Photonics"," *Fibers*, vol. 7, no. 2, p. 16, 2019.

8. M. R. A. Hassan and J. C. K. , Fei Yu, William J. Wadsworth, "Cavity-based mid-IR fiber gas laser pumped by a diode laser," *Optica*, vol. 3, no. 3, pp. 218–221, 2016.

9. V. Nampoothiri, L. Vincetti, F. B. A. Aghbolagh, B. Debord, F. Gerome, F. Benabid, and W. Rudolph, "Mid IR hollow core fiber gas laser emitting at 46 μm," *Optics Letters*, vol. 44, no. 2, p. 383, 2019.

10. L. Cao, S.-f. Gao, Z.-g. Peng, X.-c. Wang, Y.-y. Wang, and P. Wang, "High peak power 2.8 μm Raman laser in a methane-filled negative-curvature fiber," *Optics Express*, vol. 26, no. 5, p. 5609, mar 2018.

11. F. Couny, F. Benabid, and P. S. Light, "Sub-Watt Threshold CW Raman Fiber-Gas-Laser Based on H2-Filled Hollow-Core Photonic Crystal Fiber," *Physical Review Letters*, vol. 99, no. 14, p. 143903, 2007.

12. I. a. Bufetov and E. M. Dianov, "A simple analytic model of a cw multicascade fibre Raman laser," *Quantum Electronics*, vol. 30, pp. 873–877, 2007.

13. F. Benabid, G. Bouwmans, J. C. Knight, P. S. J. Russell, and F. Couny, "Ultrahigh efficiency laser wavelength conversion in a gas-filled hollow core photonic crystal fiber by pure stimulated rotational Raman scattering in molecular hydrogen," *Physical Review Letters*, vol. 93, no. 12, pp. 1–4, 2004.

14. F. Benabid, F. Couny, J. C. Knight, T. A. Birks, and P. S. J. Russell, "Compact, stable and efficient all-fibre gas cells using hollow-core photonic crystal fibres," *Nature*, vol. 434, no. 7032, pp. 488–491, 2005.

15. J. K. Brasseur, K. S. Repasky, and J. L. Carlsten, "Continuous-wave Raman laser in H_2," *Optics Letters*, vol. 23, no. 5, p. 367, 1998.

16. F. Benabid, Knight J. C., Antonopouls G., and Russell P. St. J., "Stimulated Raman Scattering in Hydrogen-filled Hollow-Core Photonic Crystal Fiber," *Science*, vol. 298, no. 5592, pp. 399–402, 2002.

17. F. Benabid, J. C. Knight, G. Antonopoulos, and P. S. J. Russell, "Stimulated Raman Scattering in Photonic Crystal Fiber," *October*, vol. 298, no. October, pp. 2000–2003, 2002.

18. V. R. Supradeepa, Y. Feng, and J. W. Nicholson, "Raman fiber lasers," *Journal of Optics (United Kingdom)*, vol. 19, no. 2, pp. 1–26, 2017.

19. Z. Li, W. Huang, Y. Cui, and Z. Wang, "Efficient mid-infrared cascade Raman source in methane-filled hollow-core fibers operating at 28 μm," *Optics Letters*, vol. 43, no. 19, p. 4671, 2018.

20. W. K. Bischel and G. Black, "Wavelength dependence of raman scattering cross sections from 200-600 nm," *AIP Conference Proceedings*, vol. 100, no. 1, pp. 181–187, 1983.

21. V. S. Averbakh, A. I. Makarov, and V. I. Talanov, "Stimulated Raman Scattering on Rotational and Vibrational Transitions in Nitrogen Gas." *Sov J Quantum Electron*, vol. 8, no. 4, pp. 472–476, 1978.

22. A. V. V. Nampoothiri, A. M. Jones, C. Fourcade-Dutin, C. Mao, N. Dadashzadeh, B. Baumgart, Y. Wang, M. Alharbi, T. Bradley, N. Campbell, F. Benabid, B. R. Washburn, K. L. Corwin, and W. Rudolph, "Hollow-core Optical Fiber Gas Lasers (HOFGLAS): a review [Invited]," *Optical Materials Express*, vol. 2, no. 7, p. 948, 2012.

23. J. W. Dawson, M. J. Messerly, R. J. Beach, M. Y. Shverdin, E. A. Stappaerts, A. K. Sridharan, P. H. Pax, J. E. Heebner, C. W. Siders, and C. Barty, "Analysis

of the scalability of diffraction-limited fiber lasers and amplifiers to high average power," *Optics Express*, vol. 16, no. 17, p. 13240, 2008.

24. V. R. Supradeepa, "Stimulated brillouin scattering thresholds in optical fibers for lasers linewidth broadened with noise," *Opt. Express*, vol. 21, no. 4, pp. 4677–4687, Feb 2013.

25. W. H. Renninger, R. O. Behunin, and P. T. Rakich, "Guided-wave Brillouin scattering in air," *Optica*, vol. 3, no. 12, pp. 1316–1319, 2016.

26. F. Yang, F. Gyger, and L. Thévenaz, "Giant brillouin amplification in gas using hollow-core waveguides," 2019.

27. C. G. Morgan, "Laser-induced breakdown of gases," *Reports on Progress in Physics*, vol. 38, no. 5, pp. 621–665, 1975.

28. A. V. V. Nampoothiri, B. Debord, M. Alharbi, F. Gérôme, F. Benabid, and W. Rudolph, "CW hollow-core optically pumped I_2 fiber gas laser," *Optics Letters*, vol. 40, no. 4, p. 605, 2015.

29. T. Bradley, G. Jasion, J. Hayes, Y. Chen, L. Hooper, H. Sakr, M. Alonso Gouveia, A. Taranta, A. Saljoghei, H. C. Mulvad, M. Fake, I. Davidson, N. Wheeler, E. Fokoua, W. Wang, S. Sandoghchi, D. Richardson, and F. Poletti, "Antiresonant hollow core fibre with 0.65 db/km attenuation across the c and l telecommunication bands," 09 2019.

30. O.-w. Bands, B. Laurent, and G. Draka, "From O to L : The Future of," no. June, pp. 83–85, 2008.

31. F. Yu, M. Cann, A. Brunton, W. Wadsworth, and J. Knight, "Single-mode solarization-free hollow-core fiber for ultraviolet pulse delivery," *Opt. Express*, vol. 26, no. 8, pp. 10 879–10 887, Apr 2018.

32. A. F. Kosolapov, A. D. Pryamikov, A. S. Biriukov, V. S. Shiryaev, M. S. Astapovich, G. E. Snopatin, V. G. Plotnichenko, M. F. Churbanov, and E. M. Dianov, "Demonstration of CO_2-laser power delivery through chalcogenide-glass fiber with negative-curvature hollow core," *Optics Express*, vol. 19, no. 25, p. 25723, 2011.

33. Barry Zhang, Walter R. Lempert and R. B. Miles, "Efficient vibrational Raman conversion in 02 and N2 cells by use of superfluorescence seeding," vol. 18, no. 14, pp. 1132–1134, 1993.

34. H. Komine and E. A. Stappaerts, "Efficient higher-Stokes-order Raman conversion in molecular gases," *Optics Letters*, vol. 5, no. 2, p. 78, 2008.

35. A. V. Gladyshev, A. N. Kolyadin, A. F. Kosolapov, Y. P. Yatsenko, A. D. Pryamikov, A. S. Biryukov, I. A. Bufetov, and E. M. Dianov, "Efficient 1.9-μm Raman generation in a hydrogen-filled hollow-core fibre," pp. 807–812, 2015.

36. Shardanand and A. D. P. Rao, "Absolute Rayleigh scattering cross sections of gases and freons of stratospheric interest in the visible and ultraviolet regions," *Nasa Tn D-8442*, vol. 1, no. March, p. 37, 1977.

REPORT DOCUMENTATION PAGE

Form Approved
OMB No. 0704-0188

1. REPORT DATE *(DD-MM-YYYY)*	2. REPORT TYPE	3. DATES COVERED *(From - To)*
03/26/2020	Master's Thesis	May 2018-Mar 2020

4. TITLE AND SUBTITLE
The Design of a Continuous Wave Molecular Nitrogen Stimulated Raman Laser in the Visible Spectrum

5a. CONTRACT NUMBER

5b. GRANT NUMBER

5c. PROGRAM ELEMENT NUMBER

6. AUTHOR(S)
Bate, Timothy J, 1st Lt USAF

5d. PROJECT NUMBER

5e. TASK NUMBER

5f. WORK UNIT NUMBER

7. PERFORMING ORGANIZATION NAME(S) AND ADDRESS(ES)
Air Force Institute of Technology
Graduate School of Engineering and Management (AFIT/EN)
2950 Hobson Way
Wright-Patterson AFB OH 45433-7765

8. PERFORMING ORGANIZATION REPORT NUMBER
AFIT-ENP-MS-20-078

9. SPONSORING/MONITORING AGENCY NAME(S) AND ADDRESS(ES)
Air Force Research Lab, Munitions Directorate
101 West Eglin Blvd
Eglin AFB, FL 32542

10. SPONSOR/MONITOR'S ACRONYM(S)
RWWS

11. SPONSOR/MONITOR'S REPORT NUMBER(S)

12. DISTRIBUTION/AVAILABILITY STATEMENT
Distribution Statement A. Approved for Public Release; Distribution Unlimited

13. SUPPLEMENTARY NOTES
This work is declared a work of the U.S. Government and is not subject to copyright protection in the United States.

14. ABSTRACT
Hollow-core photonic crystal fibers (HCPCFs) shows promise as a hybrid laser with higher nonlinear process limits and small beam size over long gain lengths. This work focuses on the design of a CW molecular nitrogen (N2) stimulated Raman laser. N2 offers Raman gains scaling up to 900 amg, scaling higher than H2. The cavity experiment showed the need to include Rayleigh scattering in the high pressure required for N2 Raman lasing. Even at relatively low pressures such as 1,500 psi, high conversion percentages should be found if the fiber length is chosen based on the pump and gain, 15 m for N2 at 1500 psi with a predicted 87% conversion of the 4.2 W coupled from the 532 nm pump.

15. SUBJECT TERMS
Stimulated Raman Scattering, laser, Hollow-core fiber, molecular nitrogen

16. SECURITY CLASSIFICATION OF:			17. LIMITATION OF ABSTRACT	18. NUMBER OF PAGES	19a. NAME OF RESPONSIBLE PERSON
a. REPORT	b. ABSTRACT	c. THIS PAGE			Glen Perram
U	U	U	UU	94	19b. TELEPHONE NUMBER *(Include area code)* (937)255-3636x4504

INSTRUCTIONS FOR COMPLETING SF 298

1. REPORT DATE. Full publication date, including day, month, if available. Must cite at least the year and be Year 2000 compliant, e.g. 30-06-1998; xx-06-1998; xx-xx-1998.

2. REPORT TYPE. State the type of report, such as final, technical, interim, memorandum, master's thesis, progress, quarterly, research, special, group study, etc.

3. DATE COVERED. Indicate the time during which the work was performed and the report was written, e.g., Jun 1997 - Jun 1998; 1-10 Jun 1996; May - Nov 1998; Nov 1998.

4. TITLE. Enter title and subtitle with volume number and part number, if applicable. On classified documents, enter the title classification in parentheses.

5a. CONTRACT NUMBER. Enter all contract numbers as they appear in the report, e.g. F33315-86-C-5169.

5b. GRANT NUMBER. Enter all grant numbers as they appear in the report. e.g. AFOSR-82-1234.

5c. PROGRAM ELEMENT NUMBER. Enter all program element numbers as they appear in the report, e.g. 61101A.

5e. TASK NUMBER. Enter all task numbers as they appear in the report, e.g. 05; RF0330201; T4112.

5f. WORK UNIT NUMBER. Enter all work unit numbers as they appear in the report, e.g. 001; AFAPL30480105.

6. AUTHOR(S). Enter name(s) of person(s) responsible for writing the report, performing the research, or credited with the content of the report. The form of entry is the last name, first name, middle initial, and additional qualifiers separated by commas, e.g. Smith, Richard, J, Jr.

7. PERFORMING ORGANIZATION NAME(S) AND ADDRESS(ES). Self-explanatory.

8. PERFORMING ORGANIZATION REPORT NUMBER. Enter all unique alphanumeric report numbers assigned by the performing organization, e.g. BRL-1234; AFWL-TR-85-4017-Vol-21-PT-2.

9. SPONSORING/MONITORING AGENCY NAME(S) AND ADDRESS(ES). Enter the name and address of the organization(s) financially responsible for and monitoring the work.

10. SPONSOR/MONITOR'S ACRONYM(S). Enter, if available, e.g. BRL, ARDEC, NADC.

11. SPONSOR/MONITOR'S REPORT NUMBER(S). Enter report number as assigned by the sponsoring/ monitoring agency, if available, e.g. BRL-TR-829; -215.

12. DISTRIBUTION/AVAILABILITY STATEMENT. Use agency-mandated availability statements to indicate the public availability or distribution limitations of the report. If additional limitations/ restrictions or special markings are indicated, follow agency authorization procedures, e.g. RD/FRD, PROPIN, ITAR, etc. Include copyright information.

13. SUPPLEMENTARY NOTES. Enter information not included elsewhere such as: prepared in cooperation with; translation of; report supersedes; old edition number, etc.

14. ABSTRACT. A brief (approximately 200 words) factual summary of the most significant information.

15. SUBJECT TERMS. Key words or phrases identifying major concepts in the report.

16. SECURITY CLASSIFICATION. Enter security classification in accordance with security classification regulations, e.g. U, C, S, etc. If this form contains classified information, stamp classification level on the top and bottom of this page.

17. LIMITATION OF ABSTRACT. This block must be completed to assign a distribution limitation to the abstract. Enter UU (Unclassified Unlimited) or SAR (Same as Report). An entry in this block is necessary if the abstract is to be limited.